

Clear sky atmosphere at cm-wavelengths from climatology data

Bartosz Lew^{1,*} and Joanna Uscka-Kowalkowska^{2,†}

¹*Toruń Centre for Astronomy, Nicolaus Copernicus University, ul. Gagarina 11, 87-100 Toruń, Poland*

²*Department of Meteorology and Climatology, Nicolaus Copernicus University, Lwowska 1, 87-100 Toruń, Poland*

(Dated: May 24, 2015)

We utilise ground-based, balloon-born and satellite climatology data to reconstruct site and season-dependent vertical profiles of precipitable water vapour (PWV). We use these profiles to numerically solve radiative transfer through the atmosphere, and derive atmospheric brightness temperature (T_{atm}) and optical depth (τ) at the centimetre wavelengths.

We validate the reconstruction by comparing the model column PWV, with photometric measurements of PWV, performed in the clear sky conditions towards the Sun. Based on the measurements, we devise a selection criteria to filter the climatology data to match the PWV levels to the expectations of the clear sky conditions.

We apply the reconstruction to the location of the Polish 32-metre radio telescope, and characterise T_{atm} and τ year-round, at selected frequencies. We also derive the zenith distance dependence for these parameters, and discuss shortcomings of using planar, single-layer, and optically thin atmospheric model approximations, in continuum radio-source flux-density measurement calibrations.

We obtain PWV- T_{atm} and PWV- τ scaling relations in the clear sky conditions, and constrain limits to which the actual T_{atm} and τ can deviate from those derived solely from the climatological data.

Finally, we suggest a statistical method to detect clear sky that involves ground-level measurements of relative humidity. The accuracy is tested using a local climatological data. The method may be useful to constrain cloud cover in cases when no other (and more robust) climatological data are available.

Keywords: radiative transfer, atmospheric effects, site testing, radio continuum: general, methods: observational

I. INTRODUCTION

Ground-based, cm-wavelengths radio continuum observations of astrophysical sources depend on atmospheric emission, and absorption of the incident radiation. Time varying line-of-sight (LOS) abundance of ice, liquid water, and water vapour generates variable optical depth, which leads to signal instabilities. These instabilities do not average out under long integrations due to the steep spectrum of atmospheric water density fluctuations. The atmospheric noise associated with dry air thermal emission, continuum and lines absorption is frequency dependent, and can be characterised by atmospheric brightness temperature ($T_{\text{atm}}(\nu)$) and transmittance ($t_{\text{atm}}(\nu)$). These atmospheric emissions contribute to the system temperature (T_{sys}) that limits the sensitivity of any ground-based telescope-receiver pair.

Over the last few decades, monitoring temperature, pressure, density, and other altitude dependent parameters of air, helped to develop few widely-accepted models of Earth atmosphere. Advances in atomic and molecular line spectroscopy provided absorption coefficients for various gas species, and computer generated spectra for mixtures of gases at given thermodynamic conditions can now reproduce these observations in great detail. Thus, the radiative properties of the atmosphere are well known, and can be derived from the first principles from radio waves to infrared frequencies.

At the cm-wavelengths the spectrum of T_{atm} is predominantly defined by continuum absorption, and emission of oxygen (O_2) and water vapour (H_2O) molecules. The lat-

ter results form strong coupling of the electric dipole moment of water molecules to the millimetre radiation via rotational transitions. Going to liquid and ice states less and no rotational freedom is possible respectively, and therefore droplets and ice particles are expected to radiate less per molecule. In the presence of clouds, the background signals are additionally attenuated in ice and droplets, which decreases the signal-to-noise ratio (SNR) of any radio source. This, translates on an increased observational time required to detect the same source at the same significance level, as compared to the situation without clouds. Given that the cloud cover is non-uniform and variable, the amount of the attenuation will change in time, generating variance at different time scales in the signal received through the main beam, or through side-lobes. For the radio continuum flux density observations at cm and mm-wavelengths, this effectively means that clear sky conditions are required.

Unlike the “dry” component of air, the distribution of atmospheric water on Earth is strongly location dependent. For this reason many dedicated radio telescopes are build at high altitudes and in a dry and/or cold climate (such as the Atacama desert or the South Pole), which reduces atmospheric emissions, maximises transmittance, improves thermal stability, and rules out clouds attenuation. At other locations, atmospheric water variations must be monitored to optimally match the observational programme to the current weather conditions. In the clear sky conditions, measurements of precipitable water vapour (PWV) can be useful to work-out optical depths and estimate atmospheric absorption corrections of astronomical radio source flux density measurements.

Atmospheric water vapour can be measured in number of ways, including (i) radio sounding, (ii) atmospheric delays of GPS-satellites signal, (iii) Sun photometry of water lines in the near-infrared light, (iv) direct radiometric measurements

*blew@astro.uni.torun.pl

†joannauk@umk.pl

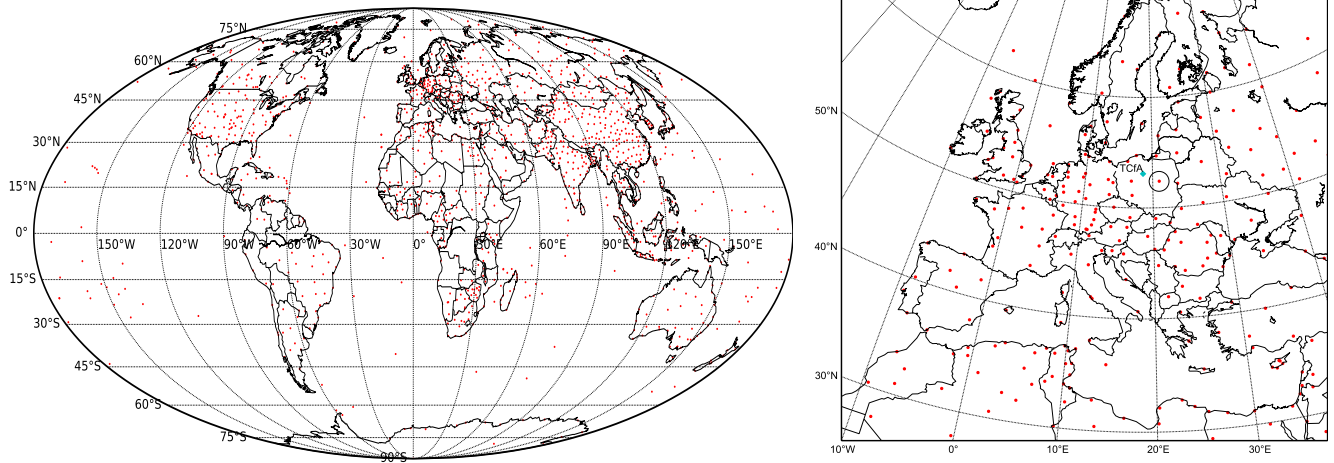


Figure 1: Global (left) and European (right) distribution of radiosonde stations with data provided by the Integrated Global Radiosonde Archive. The Legionowo station, located in Poland, is encircled. The location of Toruń Centre for Astronomy (TCfA) is marked with the cyan diamond.

in water bands (e.g. Liljegren et al. (2001)). In the larger time scales PWV can be modelled statistically using climatological data.

Currently, the publicly available data from ground-based meteorological stations, radio sounding, and satellite observations allow to reconstruct the vertical structure of atmosphere at particular location of interest. For example, the Integrated Global Radiosonde Archive (IGRA) data, which we use in this analysis, provides a substantial aerial coverage and density worldwide (Fig. 1), but only few atmospheric parameters are measured and at relatively large time intervals (only twice a day). Likewise, many satellite data obtained from solar occultation method have also nearly global coverage, but their sensitivity is largely limited in the troposphere due to clouds. However, these meteorological data can be used to model the total average PWV on month by month basis. Whether by direct radiometric observations or by solving radiative transfer equations, many radio astronomical observation sites have T_{atm} and t_{atm} calculated at the desired frequencies and the time of year (Ajello et al. 1995; Bussmann et al. 2005; Bustos et al. 2014; Radford & Holdaway 1998). In this paper we will characterise the atmosphere in these terms for the first time for the location of the 32-metre radio telescope (RT32) in Poland, and show that similar approach can be easily adapted virtually to any other location. The RT32 is one of the European VLBI Network stations, currently capable to observe in L, C, K and Ka frequency bands (see Lew et al. (2015) for more RT32 specifications). The motivation for investigating local atmosphere arises from the planned radio source survey with the 30-GHz OCRA-f focal plane, 4-pair, beam-switched receiver (Lew et al. 2015). In particular, we seek to improve the atmospheric model, previously used for the continuum flux density measurement calibrations (Gawroński et al. 2010; Lancaster et al. 2011; Peel 2010), which requires estimates of the atmospheric optical

depth (τ) at the source zenith distance (z_d). These estimates are typically obtained by performing tipping scans, with the assumption that $T_{\text{atm}}(z_d) \approx T_{\text{atm}}(0) \sec(z_d)$. We investigate limits of validity of this, and other approximations, using radiative transfer in the atmosphere in the clear sky conditions.

Radio sounding and satellite data are recorded independently of weather conditions, and modelling PWV in the clear skies requires employing selection criteria that would assure that the filtered subset of the data, indeed, corresponds to the clear sky conditions at particular location, and observation time. Search for such selection criteria, given the aforementioned sparsity and deficiencies of the sounding data, is also one of the aims of this paper.

Heuristically, a clear sky indicator could be devised by analysing the short-term stability of the solar irradiance, as measured directly in the visible light towards the Sun, or by observing the scattered radiation anywhere outside of the Sun disk. We hypothesise, that this approach could provide an assessment of the cloud cover that is independent of the observer’s judgement and will investigate this further in a separate study. However, such measurements would require pyranometers that are not available aboard weather balloons, whereas typical meteorological ground stations provide measurements of only few basic atmospheric parameters (such as temperature, pressure, dew point). Given these limitations, it is difficult (if not impossible) to infer whether the sky at the time of any given historical measurement was cloudless. With such limited amount of information one can resort to statistical treatment. Considering, for example, that typically a “good weather” coincides with high atmospheric pressure, high day-time ground temperatures (rising steadily with the Sun elevation), and relative humidity being anti-correlated with day-time temperatures, the selection by the highest temperatures and lowest RHs for a given month, should statistically pick up clear sky conditions. While we verify that this is not always

true, we demonstrate that such selection, statistically, tends to aim at the clear sky conditions with a rather low false positive fraction for the amount of provided information. While we will quantify the reliability of clouds detection using a selection criterion based on this line of reasoning (Sec. IV G), for the purpose of describing the local atmospheric model, we are going to rely on a selection criterion calibrated by external measurements of PWV.

The structure of this paper is as follows. In section II we discuss the publicly available climatological data used in our reconstructions of atmospheric profiles, describe the atmospheric model parametrisation and introduce our PWV measurements. In section III we describe the radiative transfer model used to calculate atmospheric transmittances and brightness temperatures. The main results are gathered in Sec IV. Discussion and conclusions are in sections V and VI respectively.

II. DATA

T_{atm} and t_{atm} include contributions from the dry air (with the standard nitrogen to oxygen proportions), ozone (O_3) at high altitudes, and water vapour (H_2O). Most of the atmospheric trace gases of natural and human origin including Ar, CO_2 , Ne, He, Kr, Xe, CH_4 , H_2 (NASA 1976), CO, N_2O , NO, NO_2 , N_2O_5 , HNO_3 , OCS, HCl, HF and (hydro)chlorofluorocarbons have spectra rich in lines in the sub-millimetre or infra-red (IR) range, and are relatively unimportant at the cm-wavelengths. We ignore them in the present analysis.

In the following subsections, we describe the climatological data, used to reconstruct a localised, vertical structure of the atmosphere, which is a starting point for the radiative transfer.

A. Vertical pressure and temperature profiles

We reconstruct vertical atmospheric temperature and pressure profiles using the COSPAR¹ International Reference Atmosphere project data² (hereafter CIRA86) (Rees 1988, 1992; Rees et al. 1990). These zonally-averaged data are a compilation of ground-based, radiosonde and satellite measurements of atmospheric pressure, temperature, wind velocity and geopotential height up to the altitude of $z = 120$ km, with 5° latitude resolution, roughly 2 km vertical resolution, and nearly global coverage in latitudes ($\theta = [80^\circ\text{S}, 80^\circ\text{N}]$). We use the monthly averaged vertical profiles of pressure $P(z_g)$ and temperature $T(z_g)$, given as a function of geopotential height and we apply bi-cubic interpolation in the P - θ space to obtain a profile for the desired latitude. Throughout this paper we will interpolate the profiles for the latitude $\theta_T = 53.1^\circ\text{N}$

– the latitude of TCfA (Fig. 1). Geopotential height (z_g) is related to geometrical height (z) above the sea level via:

$$z_g = \frac{R_\oplus}{R_\oplus + z} z \quad (1)$$

where $R_\oplus = 6371$ km is the assumed value of Earth radius. In what follows, we will ignore the difference between the two, as the heights are almost identical over the range of altitudes of interest. The differences are also unimportant when compared to the variance generated by the weather related pressure variations. Associating the fixed CIRA86 pressure levels to altitudes (z) allows to assign geometrical heights also to other physical quantities of interest, such as temperature, relative humidity, and mixing ratios, which are typically recorded at fixed pressure levels.

In the state of hydrostatic equilibrium the pressure profile takes form of the well-known barometric formula:

$$P(z) = P_0 \exp \left[-\frac{g_0 \mu}{RT} (z - z_0) \right], \quad (2)$$

where $g_0 = 9.80665$ km/s² is the assumed surface acceleration of the Earth, $R = 8.31432$ J · mol⁻¹ · K⁻¹ is the gas constant, $\mu = 0.0289644$ kg · mol⁻¹ is the molar mass of the air and P_0 and z_0 are fiducial pressure and altitude respectively. Since the temperature changes with altitude, the barometric formula is a poor approximation for the atmospheric pressure at high altitudes. Accounting for the temperature drops with the altitude, the formula for the pressure profile takes form of a power law (NASA 1976):

$$P(z) = P_0 \left[\frac{T_0}{T_0 + L_r(z - z_0)} \right]^{\frac{g_0 \mu}{R L_r}} \quad (3)$$

where L_r is the lapse rate (Fig. 2).

In Fig. 2 an interpolated CIRA86 pressure profiles are compared against the theoretical model (Eq. 3) with the altitude-independent lapse rate. While the consistency is very good in the troposphere, the deviation from the measured profiles in the stratosphere results from the fact that at certain altitude the denominator of Eq. 3 becomes zero and the pressure drops to zero. In reality, as one approaches tropopause the lapse rate increases to zero, the fact that we ignore in this visualisation.

In order to adjust the pressure profiles to the local conditions, and to improve the reconstruction at low altitudes ($z \lesssim 13$ km) we combine CIRA86 profile, with the profile extracted from the local sounding data (see section II B 1). However, the two profiles turn out to be quite compatible, with the largest discrepancy of $\sim 8\%$ at $z = 30$ km in January, and much less in July

Similarly, in the case of temperature profiles, we gauge the impact of the longitudinal deviations from the CIRA86 mean, by comparing it with the daytime radio sounding profile from Legionowo (near Warsaw, Poland), averaged over the period 2000-2014. We find the two datasets consistent to within 8% in the stratosphere and in the lower troposphere (Fig. 3). The consistency is better between the two regimes. The near-ground departures from the zonal averages are somewhat expected, which is why we rely on the sounding data at

¹ Committee on Space Research

² <http://badc.nerc.ac.uk/data/cira>

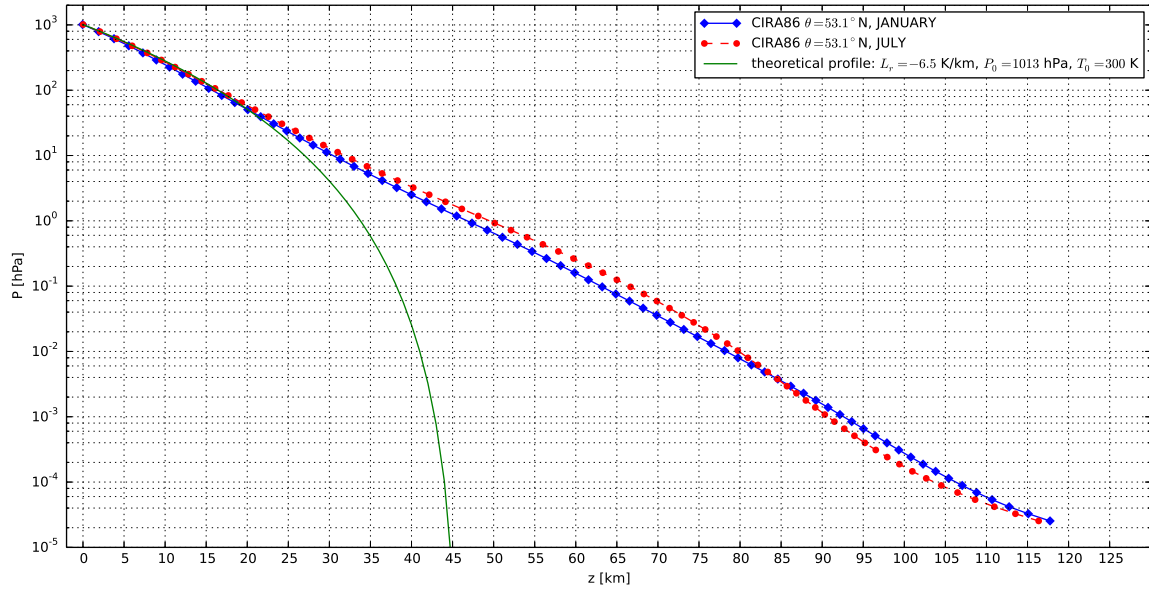


Figure 2: Atmospheric pressure profiles in January (solid, blue) and in July (dashed, red) interpolated from the CIRA86 data for the latitude $\theta_T = 53.1^\circ\text{N}$. For comparison, the theoretical profile (Eq. 3) is plotted for the assumed values of lapse-rate (L_r), pressure (P_0), and temperature (T_0) (bottom solid-green curve).

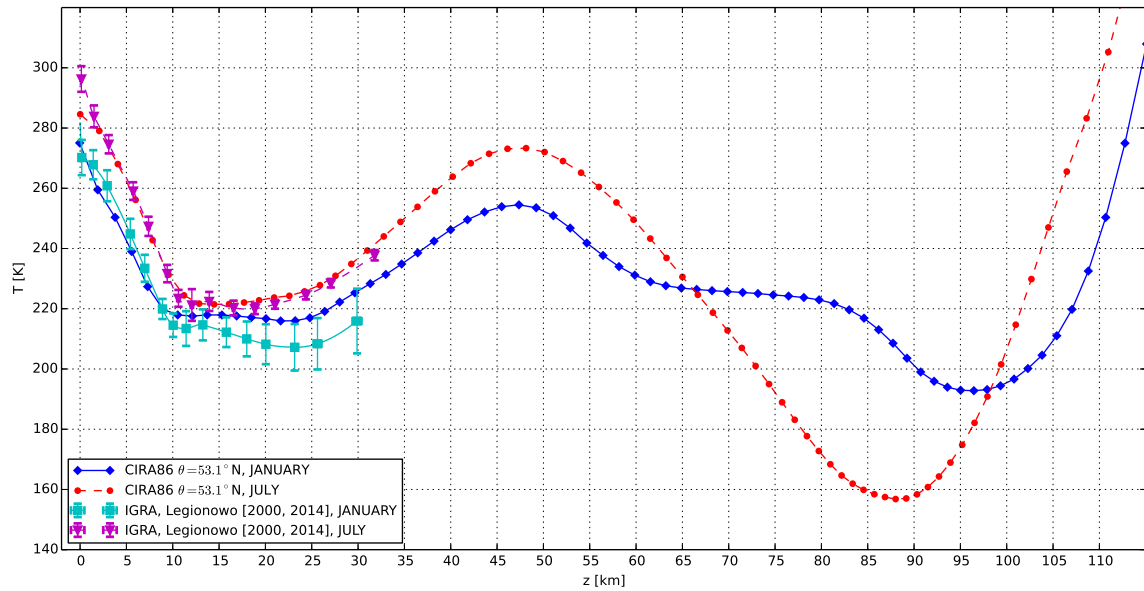


Figure 3: Atmospheric temperature profiles in January (solid, blue) and in July (dashed, red) interpolated from the CIRA86 data for the latitude $\theta_T = 53.1^\circ\text{N}$. The curves extending up to $z \approx 30$ km are the IGRA radiosonde data from Legionowo station, averaged over the period of 15 years. The horizontal error bars represent $\pm 1\sigma$ dispersion resulting from variable geopotential altitudes assigned to the fixed pressure levels. The vertical error bars represent $\pm 1\sigma$ dispersion of temperatures in the selected month.

low altitudes. The two datasets clearly mark the transition to tropopause at the altitude of about 10 km at the considered latitude.

B. Vertical WV profiles

1. Relative Humidity profiles

Of all trace atmospheric gases, WV is of the greatest relevance for the cm-wavelength observations. WV volume mixing ratio (VMR) — the number density of H₂O molecules relative to number density of all other species in the atmosphere — is highest in the troposphere. At these altitudes satellite data are no longer useful, and WV mixing ratios or alternatively the relative humidity (RH) for a given pressure and temperature, must be estimated from radio sounding data. In Fig. 1 we show the global distribution of radiosonde stations around the globe, as indexed by the Integrated Global Radiosonde Archive (Durre et al. 2006). The data is publicly available and is updated on daily basis³. As shown in Fig. 1, there are several hundreds of stations around the globe, allowing vertical profiles reconstruction with the land surface spatial resolution of order few hundreds of kilometres, on the average. The typical radiosonde accuracy to perform the temperature, pressure and RH measurement is about 0.5 °C, 1 hPa, and 1% respectively (Peixoto & Oort 1996).

For the purpose of our analysis we choose the radiosonde data from Legionowo station located near Warsaw (Poland) as it is archived since the year 1957. The data contain daily records of the geopotential height (z_g), temperature (T), dew point depression ($\Delta T_d \equiv T - T_d$, where T_d is dew point temperature) wind direction, and wind speed, probed twice a day (midnight and noon) at fixed pressure levels (P_i), as the radiosonde travels up the atmosphere. We will hereafter refer to this data as IGRA. For any given month we use the daily daytime records between and including the years 2000 and 2014. We reject the data that have incomplete or incorrect height, temperature or dew point depression information. This leaves all together a few thousand of records per month that is useful for further analyses.

At each pressure level and for each $\{T, P, T_d\}$ tuple we derive the corresponding relative humidity by analytically solving the following equation:

$$T_d(T, \text{RH}) = \frac{\lambda \Gamma(T, \text{RH})}{\beta - \Gamma(T, \text{RH})} \quad (4)$$

where

$$\Gamma(T, \text{RH}) = \ln\left(\frac{\text{RH}}{100}\right) + \frac{\beta T}{\lambda + T} \quad (5)$$

and T is in Celsius and RH is in per-cents (see e.g. Lawrence (2005) for the derivation). In Eq. 5 the constants are: $\beta = 17.62$ and $\lambda = 243.12$ °C (Sonntag 1990). These values yield T_d consistent with a more rigorous derivation of Hardy (1998) to within 0.3 °C for the temperature range from -50 °C to 50 °C, and within the measured range of relative humidities.

See also Alduchov & Eskridge (1997) to review the values of the constants from other studies.

We associate the RHs with altitudes using the reconstructed $P(z)$ relation (Sec. II A), and employ Akima interpolation (Akima 1970) to create the tabulated version of the profiles. The interpolation is performed up to the maximal altitude, however, we only use the sounding data up to $z \sim 13$ km. At larger altitudes, satellite data is used (Fig. 4). The near-ground tail of each RH profile is supplemented with the average RH data point recorded by the local meteorological station. This improves the adjustment to the RT4 site conditions.

In order to create a low-humidity subset of the data – conditions that typically correspond to a cloudless sky – we select the IGRA records according to the quantile function $Q(p_H)$ of the RH record distribution, in each of the pressure levels independently. Thus p_H becomes a selection parameter, corresponding to the probability that a random observation at any pressure level will have RH value smaller than $Q(p_H)$. In order to visualise the selection effect we arbitrarily choose $p_H = 0.1$, corresponding to the 10% driest conditions for the considered month in the year-to-year data samples: i.e. we consider records with $\text{RH} < Q(0.1)$. We will later fine tune this choice using an external data. The resulting yearly samples are averaged into a single profile that approximates the local climate in a given month. The result of the selection is shown in Fig. 4 with dashed lines.

We convert the reconstructed RH profiles into H₂O VMR profiles ($x_v(\text{H}_2\text{O})$) using the following formula:

$$x_v(\text{H}_2\text{O}) = \left(\frac{\text{RH}}{100}\right) \frac{P_{\text{sat}}(T)}{P} \quad (6)$$

where P is the total atmospheric pressure, and P_{sat} is the saturation pressure of water vapour at temperature T . P_{sat} is calculated according to the equation 10 of Murphy & Koop (2005) that is reported to be valid within the range of temperatures considered in this paper.

The reconstructed $x_v(\text{H}_2\text{O})$ profiles are shown in Fig. 4 (right panel). At large altitudes the profiles are reconstructed using the satellite data, which we discuss next.

2. Water Vapour mixing ratio profile

The Fourier Transform Spectrometer of the Atmospheric Chemistry Experiment (ACE-FTS) and the Measurement of Aerosol Extinction in the Stratosphere and Troposphere Retrieved by Occultation (MAESTRO) (Bernath et al. 2005) are two experiments aboard the Canadian SCISAT-1 satellite, flying at circular 650-km orbit with large inclination.⁴ They are dedicated to monitor the Earth atmosphere from space. Such an orbit provides almost a global coverage, enabling measurements of trace molecules abundances using spectrometry through layers of atmosphere at the satellite's sunrise and

³ <http://www1.ncdc.noaa.gov/pub/data/igra>

⁴ The Atmospheric Chemistry Experiment (ACE), also known as SCISAT, is a Canadian-led mission mainly supported by the Canadian Space Agency.

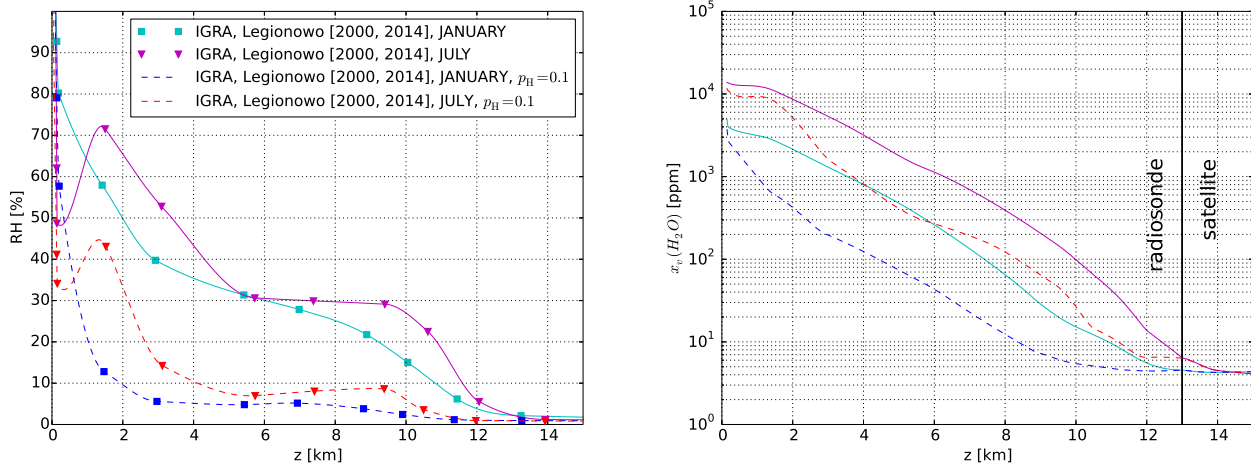


Figure 4: (*Left*) Monthly-average relative humidity profiles from Legionowo IGRA station in January (triangles) and July (squares) for the case of unscreened data (solid), and for the subset of 10% driest conditions (dashed) as indicated by $p_H = 0.1$ in the plot legend. (*Right*) The corresponding H_2O volume mixing ratio profiles. The vertical line indicates transition altitude above which the satellite data is used. The satellite water abundances are not subject to the selection criterion.

sunset (30 measurements per day), and performed towards the Sun, with the LOS tangent to the Earth’s atmosphere. The tangent LOS defines the height above the geographical location to which the measurement is assigned to. For the ACE and MAESTRO data the probed altitudes are limited by the spectrometer sensitivity at high altitudes (roughly 22 km) and by visibility of the Sun at low altitudes (Sioris et al. 2010). Due to the cloud cover, the lower altitude limit is never smaller than 5 km. The reported measurements uncertainty in H_2O is 1.3 parts per million (ppm).

SCISAT-1 is operating since August 2003 and is providing data on monthly and three-monthly basis for the range of latitudes from 85°S to 85°N (Fig. 5). ACE-FTS data used in this analysis is a compilation of measurements taken between February 2004 and February 2009, and is commonly referred to as ACE-FTS v2.2 (Jones et al. 2012).

Fig. 5 shows the ACE-FTS H_2O data that we use as a starting point for interpolations. The coverage is incomplete near the equator and in the troposphere. The difference in the seasonal WV distribution in the upper stratosphere is clearly visible. In the northern summer, the northern hemisphere exhibits larger amounts of WV as compared to the opposite hemisphere.

We construct the $x_v(\text{H}_2\text{O})$ profile by interpolating the ACE-FTS mixing ratios across latitudes at each pressure level. We then cross-interpolate the mixing ratios at the selected latitude θ_T , and obtain the $x_v(\text{H}_2\text{O})$ pressure dependence, which is next converted to altitude dependence using the CIRA pressure-altitude relation (Sec. II A). The result is shown in Fig. 6.

We combine the satellite $x_v(\text{H}_2\text{O})$ profiles with the tropospheric radiosonde profiles by sewing them using a linear transformation from one profile to another in the range of overlapping altitudes (typically $10 \lesssim z \lesssim 13$ km).

Various satellite WV data seem to be consistent. For ex-

ample, Thomason et al. (2004) reports consistency of WV VMRs from SAGE⁵ II and HALOE⁶ satellites. ACE data (which is used in this analysis) have also been compared with SAGE II and HALOE results, and were found compatible to within $O(10)\%$ (Carleer et al. 2008; Velazco et al. 2011; Walker et al. 2005). Although these measurements are to a large extent consistent with each other, the global distribution of the RH is not exactly zonally uniform: i.e. some longitudinal dependence is possible. However, the crucial impact on the radiative transport in the Ka-band is due to the tropospheric WV content, and it is clear that any stratospheric longitudinal variations of VMRs of WV and ozone should have a minor effect on the column abundances, and consequently, a minor impact on the radiative transfer calculations.

C. Ozone

We model the local atmospheric ozone VMR profile using a combination of ozonesonde and satellite data⁷ provided by the Royal Netherlands Meteorological Institute (hereafter KNMI). The KNMI ozone data are zonally averaged VMRs measured over 17 different latitudes from -80°S to 80°N , and at 19 different pressure levels from 0.3 hPa to 1000 hPa. The data is compiled from 30 ozone stations and SBUV-SBUV/2 satellite observations, collected during the years 1980-1991 (Paul et al. 1998).

Currently, there is a wealth of ozone data from many

⁵ Stratospheric Aerosol and Gas Experiment II

⁶ Halogen Occultation Experiment

⁷ http://www.knmi.nl/research/climate_chemistry/Data/FKClimatology/

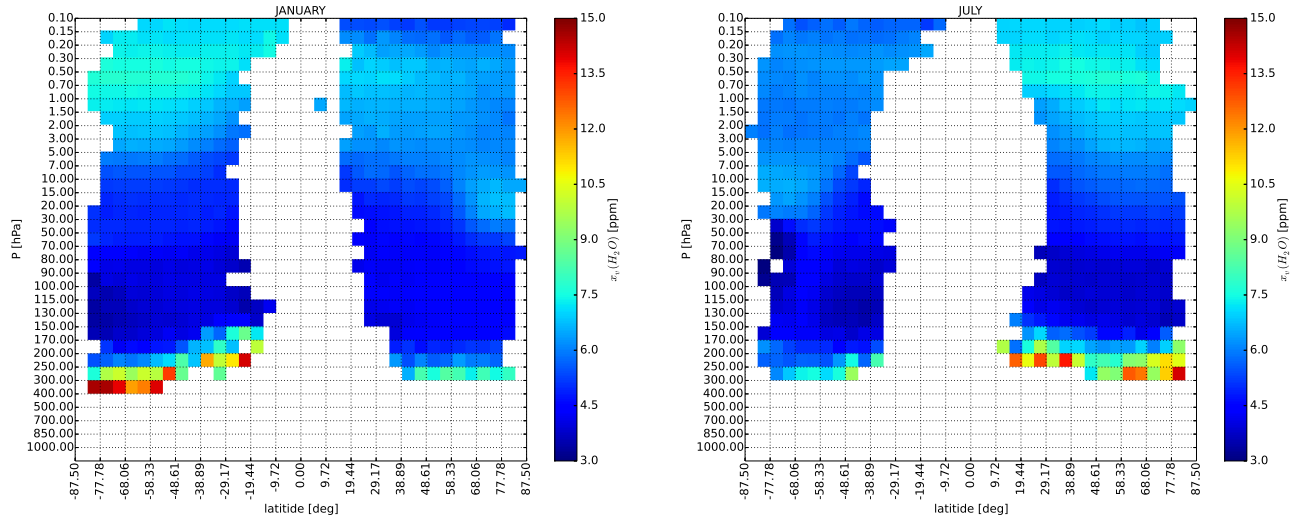


Figure 5: Hemispherical distribution of water vapour volume mixing ratio from ACE-FTS v2.2 (see text), as a function of latitude and pressure in January (left) and July (right).

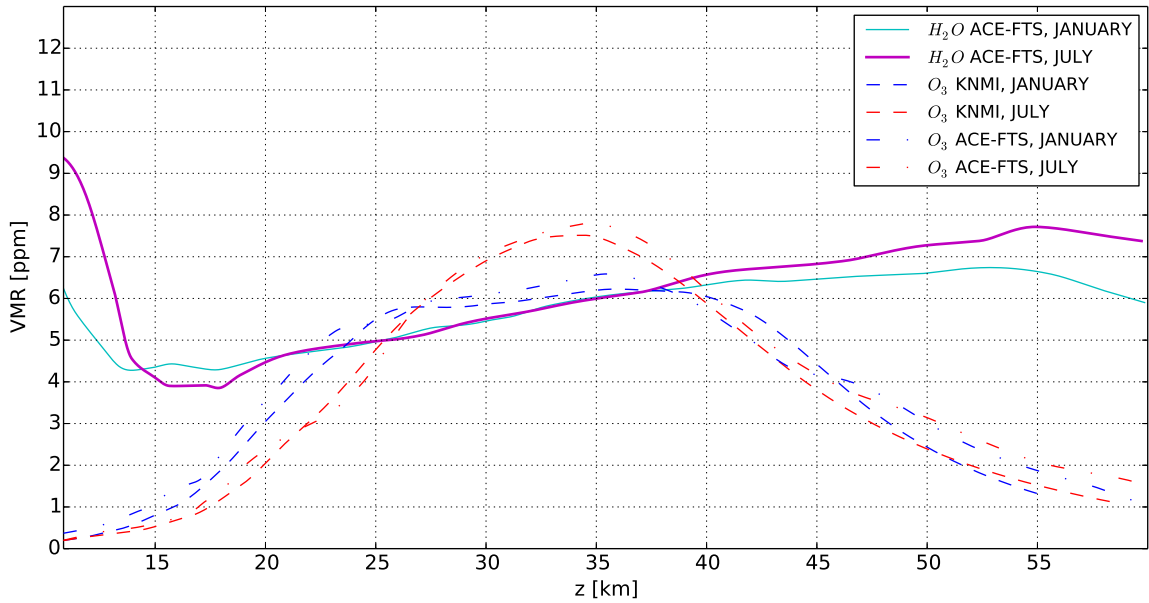


Figure 6: WV volume mixing ratio profiles (solid) interpolated at $\theta_T = 53.1^\circ\text{N}$ from ACE-FTS data (Fig. 5) in January (cyan, thin) and July (magenta, thick). The dashed (dash-dotted) lines represent the ozone VMR profiles interpolated from the KNMI (ACE-FTS) data (Fig. 7) in January (blue) and July (red) (see Sec. IIC).

satellites and from radiosondes (e.g. Fioletov et al. (2002); Jones et al. (2012); WOUDC (1961)) that continuously monitor the ozone layer. In the current work, our main focus is on the cm-wavelengths, where the ozone impact is sub-dominant, but for the sake of completeness and accounting for possible extensions into a higher frequencies, we include one of the available ozone datasets (KNMI) into the analysis. As an example of ozone data cross-experiment compatibility, we com-

pare (Fig. 7) the KNMI measurements (top panels) with the ACE-FTS data (bottom panels). The latter have a larger spatial resolution, but incomplete coverage. The consistency between the interpolated profiles is also shown in Fig. 6.

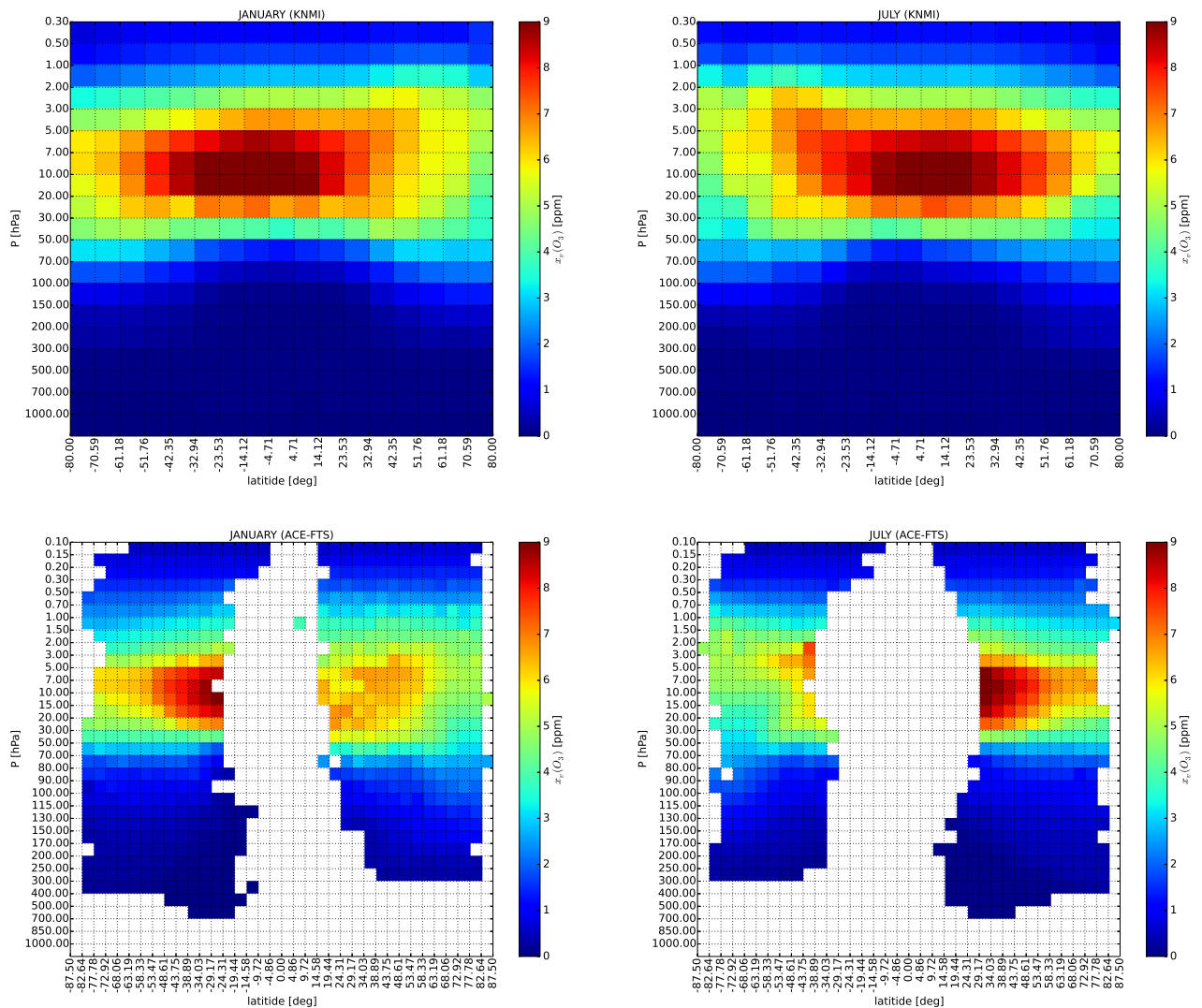


Figure 7: Hemispherical distribution of ozone volume mixing ratio as a function of latitude and pressure level as given by KNMI compilation (top panels) and by ACE-FTS satellite measurements (bottom panels) in January (left panels) and in July (right panels).

D. Ground-level meteorological data

We improve the adjustment of the atmospheric model to the local conditions at the ground-level by including data recorded by the IRDAM WST7000 meteorological station, installed on the roof of TCfA, nearby RT32. The data include temperatures, pressures, and relative humidities recorded at a high time resolution. We used the data covering the period of slightly exceeding 4 years i.e. from October 2010 to November 2014. In each month they contribute as a single data point in the RH profile (Fig. 4) at the altitude of TCfA, but also influence higher altitudes via smooth interpolation. We detect a systematic effect in this RH dataset, resulting from a progressive deterioration of the humidity sensor over time. The effect leads to an overestimation of the local RHs by $< 4\%$ in the years 2011 and 2014 as compared to the values from

2012, and less than that in the year 2013.⁸ In our analysis we ignore these systematical effects as they are thought to be unimportant.

E. Data selection criteria and model parametrisation

We are interested in deriving a localised, mean T_{atm} and t_{atm} as a function of month in the clear sky conditions. Using an unfiltered data, that we discussed in Sec. IIB 1 and Sec. IID, would lead to a biased results because only a frac-

⁸ In the end of 2011 the station was renewed, hence in 2012 it provided the least biased readouts. Therefore, the previous and the following years are biased to a greater extent.

tion of the data is obtained at the times when there is no cloud cover. The fraction of time with clear sky conditions, depends on the location of interest and on the time of year. In particular, in the lowlands surrounding RT32 observing site the fraction of days with the mean daily cloud cover $\leq 20\%$ ranges from $\sim 9\%$ to $\sim 11\%$, on the average (Woś 2010).

As discussed in Sec. I, there is an anti-correlation between RH and solar irradiance, which could statistically hint on clear sky conditions, if one selects data by low, ground-level RHs. Observations indicate however, that during the most cloudy months such selection criteria returns a considerable false-positive rates, as discussed in Sec. IV G. However, there is another complication regarding this selection scheme. The correlation between water vapour content at the ground level and that at larger altitudes is rather weak, or non-existent. Some correlation exists only between the neighbouring pressure levels in the lower troposphere. For this reason, the parametrisation of the selection criterion by low RHs at a single, fixed pressure level lacks a very desired feature: that the mean column PWV should decrease monotonically as one straitens the selection criterion.

Since we are interested in an assessment of the brightness temperature in the conditions that are *statistically* compatible with the clear sky situation in terms of the column PWV content, we will filter the data coherently at all pressure levels. For a given month and year, we use only the IGRA records that yield

$$\text{RH} < Q_{\text{RH},i,j}(p_{\text{H}}), \quad (7)$$

where $Q_{\text{RH},i,j}(p_{\text{H}})$ is the quantile function of the RH distribution at i 'th pressure level in j 'th month. We use the same p_{H} parameter consistently for every pressure level, month, and for the ground-based meteorological data. The resulting vertical profile will be, in most cases, a combination of data taken at different days, but the parametrisation assures that imposing a stronger selection criterion (i.e. lowering p_{H}) results in a lower column PWV, as expected. In order to average over the year-to-year variability of PWV, and approximate the climate for a given month, we split the IGRA records into yearly subsamples, which we analyse separately. For a given month, the average RH value at i 'th pressure level is taken as the mean RH from all years. The exact value of the p_{H} selection parameter, that would be compatible with cloudless skies, and would not select only the driest conditions, is unknown, but can be constrained by independent PWV measurements, performed in the clear sky conditions (see Sec. II F).

The downside of such parametrisation is that the probability distribution function (PDF) for the p_{H} selection parameter, by construction, is zero outside of $[0, 1]$ range. This is because p_{H} is associated with the probability of obtaining a RH measurement smaller than the quantile function (Eq. 7) in a given pressure level, month and year. The final monthly-average profile is a multi-year mean, therefore even for the maximal value of $p_{\text{H}} = 1$ – i.e. when no data is filtered out – the resulting average model will not be able to describe an individual day with PWV values above the mean. In the current approach we are however focused on a parametrisation that is suitable for the average clear sky model, and will accept these

limitations since we are not going to analyse the significance of deviations of individual measurements from the mean.

In order to account for the large diurnal variation of RH, and to enable a meaningful comparison between different days, we select the RH data records acquired between hours 10 and 14 (UTC+1), where the temperatures should be least affected by the diurnal variation of the solar irradiance. Hence, the differences in RH between different days, better reflect the actual PWV content variations, and not temperature variations.

F. PWV measurements

We have been monitoring PWV, expressed in column millimetres of water (w), in the clear sky conditions since June 2013. A compilation from the first data release is summarised in Tab. I. The measurements were performed using a handheld MICROTUPS II Sun photometer at the Meteorological Observatory of the Nicolaus Copernicus University in Toruń (hereafter DMC). In what follows, we will refer to our Sun photometer PWV measurements as *TR-PWV-DR-1*.

The atmospheric column PWV is calculated along LOS towards the Sun, based on photometric measurements of water absorption peak at 936 nm, and of the continuum at 1020 nm (without water absorption). The PWV resulting from Beer-Lambert-Bouguer's law is converted to the zenith column water abundance based on the Sun zenith distance at the time and location of the measurement. The accuracy of the measurement is 0.1 mm. Using a reference MICROTUPS II Sun photometer we verified that with the factory settings the systematical differences to measure PWV between different instruments is $\Delta w \lesssim 0.1$ mm.

The data have been collected only in the clear sky conditions, which allows to quantify the PWV variations due to air masses carrying different amounts of water vapour depending on seasons and winds. The data are typically recorded every hour and each recording session contains several measurements that are averaged. In the stable clear sky conditions the differences between hourly samples are small (relative to our measurement precision) and we use a daily mean as a single data record. Then, the monthly average, standard deviation and the extreme values are calculated from daily records (Tab. I).

We also utilise the publicly available PWV data from the AERONET⁹ robotic stations, which automatically trace the Sun and measure the atmospheric water lines spectrum. We use the data from Belsk station in Poland (near Warsaw), collected between (and including) years 2002 and 2014. Since the AERONET data are collected automatically and exclude only the periods of rain, the raw data may be contaminated by the presence of clouds and therefore should be more compatible with the average PWV abundances reconstructed from climatology data: i.e. without imposing any selection criteria.

⁹ <http://aeronet.gsfc.nasa.gov>

AERONET data is essentially provided at three levels of post-processing. Level 1.0 is the raw data (Fig. 8). AERONET level 1.5 data are automatically screened for clouds based on number of simple criteria involving time and spectral stability of the measured optical depths (Smirnov et al. 2000). Level 2.0 data, which we use in our analysis, are further manually corrected for glitches and any other abnormalities that could elude automatic screening.

The difference between our measurements and the AERONET data level 2.0 (Fig. 8) is that the latter have clouds removed directly from the LOS towards the Sun, thus not guaranteeing a cloudless sky. Our sample however, in most cases was taken during cloudless days, at the penalty of fewer measurements.

III. SOLVING RADIATIVE TRANSFER THROUGH ATMOSPHERIC LAYERS

In this section we briefly review the principal equations of the radiative transfer in the atmosphere, and outline the calculation setup.

Given a model of the vertical structure of the atmosphere we calculate the column PWV, T_{atm} , t_{atm} , and the corresponding optical depth (τ) at the cm-wavelengths using the AM program (version 7.2) – a publicly-available radiative transfer solver, developed at the Harvard-Smithsonian Center for Astrophysics (Paine 2012).

Propagation of radiation through a medium is given by the radiative transfer equation

$$\frac{dI_\nu}{ds} = -\kappa_\nu I_\nu + \epsilon_\nu, \quad (8)$$

where I_ν is the specific intensity and κ_ν is the total opacity due to absorption and scattering:

$$\kappa_\nu = -\frac{d\tau_\nu}{ds}, \quad (9)$$

τ_ν is the optical depth, and ϵ_ν is the emissivity along the propagation path s . All quantities are, in general, frequency dependent as indicated by index ν . In the case of local thermodynamic equilibrium (LTE) the radiative transfer equation can be rewritten (Wilson et al. 2009) as:

$$-\frac{1}{\kappa_\nu} \frac{dI_\nu}{ds} = \frac{dI_\nu}{d\tau} = I_\nu - B_\nu(T), \quad (10)$$

where $B_\nu(T)$ is the Planck radiance. The solution is given by:

$$I_\nu(s) = I_\nu(0)e^{-\tau_\nu(s)} + \int_0^{\tau(s)} B_\nu(T(\tau))e^{-\tau_\nu} d\tau. \quad (11)$$

For a thin atmospheric layer, where the temperature can be assumed constant, Eq. 11 can be integrated as

$$I_\nu(s) = I_\nu(0)e^{-\tau_\nu(s)} + B_\nu(T)(1 - e^{-\tau_\nu(s)}), \quad (12)$$

where the first term in the right hand side is the incident radiance that is exponentially attenuated along the propagation

path. The second term amounts to the thermal emission of the layer corrected for the self-absorption, required to maintain the assumed LTE. The spectrum of the optical depth is medium dependent and can be derived from the quantum-mechanical properties of atoms and molecules present in the medium. The effects leading to violation of the LTE, such as thermal conduction or convection are reasonably neglected.

The radiative transfer equation is solved through $N_L = 300$ stacked atmospheric layers, each characterised by its pressure (P), temperature (T), geometrical thickness, and chemical composition: a mixture of nitrogen, oxygen, ozone, and water vapour defined in terms of VMRs. The layers are homogeneously distributed in log-altitude space, which roughly corresponds to a homogeneous distribution in pressure space. We use the same definition of layers for all atmospheric species. The lowermost layer altitude, $z = 133$ m, is chosen to coincide with the altitude of the RT32. The uppermost layer altitude is assumed to be $z_{\text{max}} = 60$ km.

It is assumed that the incident (background) radiation has initially Planckian distribution ($B_\nu(T)$) with $T = T_{\text{CMB}} = 2.726$ (Fixsen 2009), the thermodynamic temperature of the Cosmic Microwave Background radiation (CMB). Thus, our definition of T_{atm} includes the contribution of CMB.

For each absorbing (emitting) species and for each layer in the atmosphere, the radiative transfer equation is solved. The optical depth for i 'th layer is therefore a sum of optical depths over all absorbing species:

$$\tau_i(\nu) = \sum_j \tau_{ij}(\nu). \quad (13)$$

The optical depth is calculated for each species accounting for the spectral line parameters from HITRAN database, and based on the thermodynamical properties of gas in the layer (its temperature and pressure).

For i 'th layer the radiative transfer equation is defined as follows (Paine 2012):

$$I_i(\nu) = I_{i-1}(\nu)e^{-\tau_i} + B(\nu, T_i)(1 - e^{-\tau_i(\nu)}) \quad (14)$$

where $I_i(\nu)$ is the incident radiance at the lower boundary of the i 'th layer and $I_{i-1}(\nu)$ is the incident radiance at the lower boundary of the previous layer (located up in the atmosphere). The thermodynamic temperature T_i is the temperature in the middle of the i 'th layer and $B(\nu, T_i)$ is the Planck radiance:

$$B(\nu, T_i) = \frac{2h\nu^3}{c^2} \frac{1}{e^{\frac{h\nu}{k_B T_i}} - 1} \quad (15)$$

Calculations are performed towards zenith or at directions located at zenith distance z_d , and layers are assumed to have flat geometry. We record the total brightness temperature (T_{atm}), Rayleigh-Jeans (RJ) temperature (T^{RJ}), optical depth (τ) and the corresponding transmittance ($t_{\text{atm}} = e^{-\tau}$) as a function of frequency and the column PWV (w). The brightness temperature T_{atm} is obtained by solving

$$I_{\nu, \text{atm}} = B_\nu(T_{\text{atm}}) \quad (16)$$

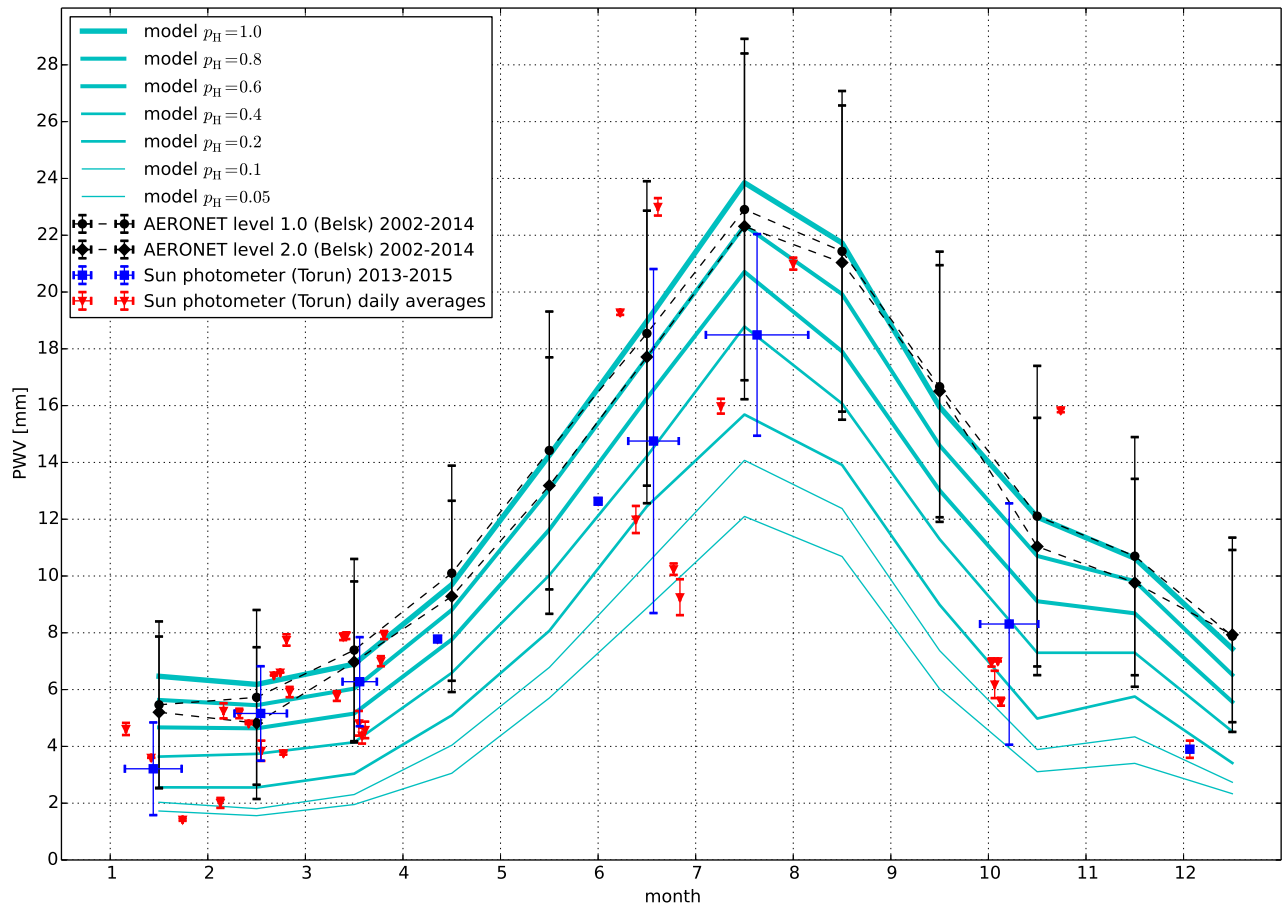


Figure 8: A compilation of PWV measurements. The monthly averages from our *TR-PWV-DR-1* sample are marked with blue squares while the daily averages are marked with red triangles. The error bars correspond to $\pm 1\sigma$ deviation from the mean. The black diamonds (dots) are the AERONET data level 2.0 (1.0) from Belsk station. The blue lines represent our PWV model reconstructed from climatology data described in Sec. II. The thickness of the individual solid lines increases with p_H . The increases correspond to progressively less aggressive selection of the climatology data by low RH values (Sec. II E).

where $I_{\nu,\text{atm}}$ is the output radiance at the lowermost atmospheric layer. Analogously the RJ temperature is calculated from the Rayleigh-Jeans relation:

$$I_{\nu,\text{atm}} = \frac{2k\nu^2}{c^2} T^{\text{RJ}} \quad (17)$$

We calculate the spectrum of atmospheric emission within the frequency range $\nu = [1, 60]$ GHz with 50 MHz resolution. Details of the physical processes taken into account are described in the AM program technical memo (Paine 2012).

IV. RESULTS

A. Precipitable Water Vapour

A compilation of the *TR-PWV-DR-1* measurements (Sec. II F) is shown in Fig. 8, and the corresponding data are

gathered in Tab. I. In this figure the cyan solid lines represent the PWV models reconstructed from the climatology data discussed in Sec. II A– II D. The line width increases as the p_H selection parameter increases (Sec. II E). For any given month, the reconstructed column PWV is assumed to occur at mid-month.

We constrain the value of the p_H parameter, which implies the PWV level that is expected to occur in the clear sky conditions. We use a χ^2 minimisation, neglecting the cross-month covariance:

$$\chi^2 = \sum_{i=1}^{12} [\langle w \rangle_i - \mathcal{M}_i(p_H)]^2 / \sigma_i^2, \quad (18)$$

where $\langle w \rangle_i$ and σ_i^2 are the i 'th month PWV mean and standard deviation respectively, and $\mathcal{M}_i(p_H)$ is the model PWV value interpolated at the locus of the i 'th month data point. When the monthly variance estimate is unknown (due to missing data), it is interpolated from the neighbouring months (with

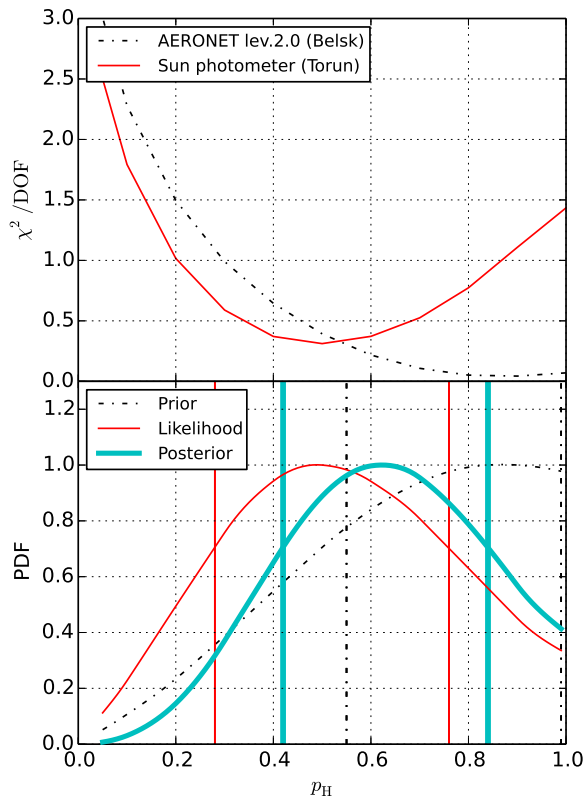


Figure 9: Constraints on p_H selection parameter (see Sec. II E). The vertical lines in the bottom panel encompass the 68% CR, as summarised in Tab. II. The three PDFs are obtained from the AERONET/Belsk PWV data (black, dash-dotted), Toruń MICROTOPS measurements (red, solid thin), and the two datasets combined (solid thick).

continuity across Dec/Jan).

Given the PWV data \mathcal{D} , and the reconstructed PWV model \mathcal{M} , parametrised by p_H , we define the posterior probability for p_H using the Bayes theorem:

$$\mathcal{P}(p_H|\mathcal{M}, \mathcal{D}) \propto \mathcal{L}(\mathcal{D}|\mathcal{M}, p_H)\Pi(p_H|\mathcal{M}) \quad (19)$$

where $\mathcal{L}(\mathcal{D}|\mathcal{M}, p_H)$ is the likelihood of the data given the model and $\Pi(p_H|\mathcal{M})$ is the prior imposed on the parameter probability distribution function (PDF). By construct the PDF for the p_H parameter is zero outside $[0, 1]$ region (see Sec. II E). We assume the AERONET data as a prior and obtain the maximum posterior constraint on the p_H parameter and calculate the 68% confidence interval. The likelihood function is probed using the Sun photometer data (Fig. 9). However, we also analyse each of the datasets alone. Constraints on the p_H parameter are gathered in Tab. II. As indicated by the vertical lines in Fig. 9, *TR-PWV-DR-1* and the AERONET/Belsk datasets are compatible at the 68% CL, but the maximum-likelihood p_H parameter value is lower for the earlier data, which we attribute to the fact that the *TR-PWV-DR-1* sample was collected during excellent weather condi-

Table I: Compilation of column PWV measurements (*TR-PWV-DR-1*) performed in the clear sky conditions using MICROTOPS II Sun photometer (Sec. II F).

Location ^a	18° 34' 04.8" E, 53° 01' 12.0" N				
Period	2013/06/07 – 2015/04/13				
Duration ^b	~ 17 months				
Month	$\langle w \rangle^c$ [mm]	min/max ^d [mm]	# of days ^e	Comment ^f	
1	3.2 ± 1.6	1.4 / 4.6	3		
2	5.2 ± 1.7	2.0 / 7.7	10		
3	6.3 ± 1.6	4.4 / 7.9	8		
4	7.8 ± 0.1	7.8 / 7.8	1	SD	
5	12.6 ± 0.1	12.6 / 12.6	1	SD	
6	14.8 ± 6.1	9.3 / 23.0	5		
7	18.5 ± 3.5	16.0 / 21.0	2		
8			0	ND	
9			0	ND	
10	8.3 ± 4.2	5.6 / 15.8	5		
11			0	ND	
12	3.9 ± 0.1	3.9 / 3.9	1	SD	

^aGeodetic coordinates of the observation site (DMC).

^bEffective number of observed months. No-observation periods: Aug–Sep 2013 and Jul–Oct 2014.

^cMonthly average and a standard deviation of PWV, both calculated using daily means.

^dPWV data extremal values

^eThe total number of days observed in a given month.

^fSD - single day mean and standard deviation, ND - no data

tions, which guaranteed a cloudless sky, and therefore statistically favoured lower PWV abundances.

From Fig. 8 it is clear that AERONET/Belsk PWV distribution year-around follows very closely the shape of the reconstructed models with high p_H values (corresponding to weak data selection). The strength of the correlation is also reflected in the smallness of the best fit χ^2/DOF value, although the dispersion of the individual PWV measurements (from which the monthly variance is calculated) is relatively large in both data samples. Clearly, AERONET/Belsk level 1.0 dataset corresponds to a larger p_H value than level 2.0 dataset, as expected.

B. Average clear sky atmospheric brightness temperature and optical depth: case for Toruń, Poland

Using the reconstructed, vertical structure of atmosphere (Sec. II) we now determine the local T_{atm} and τ using the radiative transfer solver described in Sec. III.

In Fig. 10 we plot the best-fit local T_{atm} models up to the Q-band frequencies. The most prominent atmospheric feature is associated with the water line that is Doppler and pressure broadened about the resonance frequency $\nu_0 \approx 22.235$ GHz. On the top of the broad band emission a very weak and sharp contribution due to thermally-excited stimulated emission is found. This is seen as a tiny increase of $\Delta T_{\text{atm}} \approx 0.15$ K exactly at the resonance frequency ν_0 , however effects of fluctuating PWV levels due to atmospheric turbulence (see

Table II: 68% CL constraints on p_H selection parameter from the Sun photometer data (Tab. I), from the AERONET/Belsk data and from the two datasets combined.

	Sun Photometer (Toruń)	AERONET lev. 2.0 (Belsk)	Combined
$\min(\chi^2/\text{DOF})$	~ 0.31	~ 0.04	NA
p_H Confidence Range	(0.28, 0.76)	(0.55, 1.00)	(0.42, 0.84)
MOD(p_H)	$0.49^{+0.27}_{-0.21}$	$0.87^{+0.12}_{-0.32}$	$0.62^{+0.22}_{-0.20}$
EX(p_H)	0.53	0.65	0.62

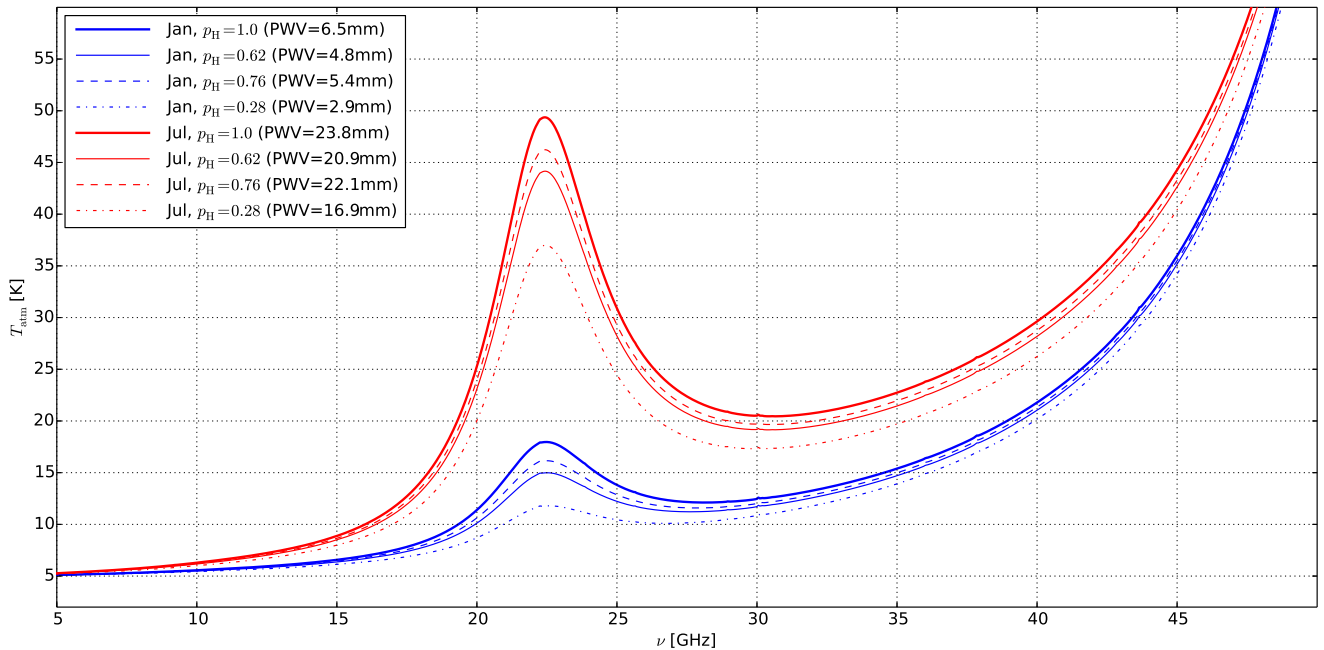


Figure 10: Average atmospheric brightness temperature as a function of frequency. The upper (red) lines correspond to July and lower (blue) lines correspond to January in Toruń. Within each group the thick solid line traces T_{atm} corresponding to the model obtained without imposing any selection criteria on the climatology data ($p_H = 1.0$). Thin solid lines are calculated according to the best fit models found using the combined (Toruń + AERONET/Belsk) PWV data samples. The best fit p_H selection parameter values are given in the plot legend and in Tab. II. The dashed and dash-dotted lines enclose the 68% confidence region, derived using the Toruń PWV data sample alone (*TR-PWV-DR-1*). All curves are calculated for the zenith distance $z_d = 0^\circ$ at the RT32 altitude ($z = 0.133$ km).

Sect. IV E) generate T_{atm} variations of the same order in the time scale of hours or less.

Clearly, T_{atm} and τ are strongly season dependent as is the level of PWV. The high-frequency tail of T_{atm} in Fig. 10 is caused by the contribution from the oxygen O_2 line that is insensitive to PWV content. The only way to mitigate this emission is to observe at larger altitudes, i.e. through a thinner atmosphere. In Fig. 10 the legend provides the column PWV in millimetres for each model. For comparison, the mean PWV level at the South Pole in austral winter is about 0.26 mm (Bussmann et al. 2005) which is ~ 25 times smaller as compared to the mean PWV content in January in Legionowo (Poland) and ~ 12 times smaller than the mean PWV content in the clear sky conditions measured in Toruń (Tab. I).

The impact of ozone is seen only in spectral lines, which are weak in the Q-band, as compared to the effects caused by atmospheric instabilities. We re-calculate the spectra with the resolution of 5 kHz and observe that the lines amplitude

is well below 1 K above the continuum at the resonance frequencies. The ozone contribution becomes more important however, at higher frequencies.

From Fig. 10 it is clear that lower PWV levels result in lower T_{atm} values. The stratospheric PWV levels, as traced by satellites, are roughly constant throughout the year. We observe that above 13 km the levels are very small, the order of few μ -meters: $w \sim 0.005$ mm in January and July, and therefore the stratospheric PWV impact on T_{atm} seems unimportant for the ground level sites.

We use the best fit model determined by the combined AERONET/Belsk and Toruń data samples (Tab. II) to calculate the local T_{atm} and τ for each month. The result is shown in Tab. III. In that table the error bars correspond to the variation of the p_H selection parameter within the 68% CR.

Table III: 68% CL constraints on the clear sky, zenith, mean atmospheric brightness temperature (T_{atm}) and optical depth (τ). The values for the selected frequencies and months are calculated according to the best fit PWV model selected by the combined AERONET/Belsk and Toruń data samples (Tab. II). The asterisk (*) marks the errors that are rounded up to appear non-zero at the provided precision. A and B are the linear-fit constants of the $T_{\text{atm}} = A\langle w \rangle + B$ and $t_{\text{atm}} = A\langle w \rangle + B$ scaling relations. A and B are written in scientific notation with the decimal exponent in parentheses.

ν [GHz]	5	15	22	30	5	15	22	30	
Month	$\langle w \rangle$ [mm]	T_{atm} [K]	T_{atm} [K]	T_{atm} [K]	T_{atm} [K]	τ $\times 10^{-3}$	τ $\times 10^{-2}$	τ $\times 10^{-2}$	τ $\times 10^{-2}$
1	4.8 ^{+1.1} _{-1.0}	5.10 ^{+0.01} _{-0.01}	6.4 ^{+0.1} _{-0.1}	14.6 ^{+1.9} _{-1.7}	11.7 ^{+0.5} _{-0.5}	9.50 ^{+0.03} _{-0.03}	1.5 ^{+0.1} _{-0.1}	4.7 ^{+0.8} _{-0.7}	3.6 ^{+0.2} _{-0.2}
2	4.7 ^{+0.9} _{-0.9}	5.09 ^{+0.01} _{-0.01}	6.3 ^{+0.1} _{-0.1}	14.4 ^{+1.5} _{-1.5}	11.7 ^{+0.4} _{-0.4}	9.48 ^{+0.03} _{-0.04}	1.4 ^{+0.1*} _{-0.1*}	4.6 ^{+0.6} _{-0.6}	3.6 ^{+0.2} _{-0.2}
3	5.3 ^{+1.0} _{-1.0}	5.09 ^{+0.01} _{-0.01}	6.4 ^{+0.1} _{-0.1}	15.5 ^{+1.7} _{-1.7}	11.9 ^{+0.5} _{-0.5}	9.39 ^{+0.04} _{-0.04}	1.5 ^{+0.1} _{-0.1*}	5.0 ^{+0.7} _{-0.7}	3.6 ^{+0.2} _{-0.2}
4	7.8 ^{+1.2} _{-1.2}	5.12 ^{+0.01} _{-0.01}	6.7 ^{+0.2} _{-0.1}	19.9 ^{+2.1} _{-1.9}	13.0 ^{+0.6} _{-0.6}	9.34 ^{+0.06} _{-0.06}	1.5 ^{+0.1} _{-0.1}	6.6 ^{+0.9} _{-0.8}	4.0 ^{+0.2} _{-0.2}
5	11.8 ^{+1.6} _{-1.6}	5.16 ^{+0.02} _{-0.02}	7.3 ^{+0.2} _{-0.2}	26.9 ^{+2.8} _{-2.8}	14.9 ^{+0.7} _{-0.7}	9.36 ^{+0.07} _{-0.07}	1.7 ^{+0.1} _{-0.1}	9.3 ^{+1.1} _{-1.1}	4.6 ^{+0.3} _{-0.3}
6	16.3 ^{+1.7} _{-1.9}	5.20 ^{+0.02} _{-0.02}	7.9 ^{+0.2} _{-0.2}	34.7 ^{+3.0} _{-3.3}	17.0 ^{+0.8} _{-0.9}	9.40 ^{+0.08} _{-0.07}	1.9 ^{+0.1} _{-0.1}	12.3 ^{+1.3} _{-1.4}	5.4 ^{+0.3} _{-0.3}
7	20.9 ^{+1.9} _{-1.9}	5.25 ^{+0.02} _{-0.02}	8.5 ^{+0.2} _{-0.2}	42.8 ^{+3.2} _{-3.2}	19.2 ^{+0.9} _{-0.8}	9.47 ^{+0.08} _{-0.07}	2.1 ^{+0.1} _{-0.1}	15.5 ^{+1.4} _{-1.4}	6.1 ^{+0.3} _{-0.3}
8	18.1 ^{+2.4} _{-1.8}	5.23 ^{+0.02} _{-0.02}	8.1 ^{+0.3} _{-0.2}	38.0 ^{+4.0} _{-3.2}	17.9 ^{+1.1} _{-0.8}	9.43 ^{+0.08} _{-0.07}	2.0 ^{+0.1} _{-0.1}	13.6 ^{+1.7} _{-1.4}	5.7 ^{+0.4} _{-0.3}
9	13.0 ^{+1.9} _{-1.7}	5.18 ^{+0.02} _{-0.02}	7.5 ^{+0.2} _{-0.2}	29.0 ^{+3.3} _{-2.9}	15.5 ^{+0.8} _{-0.8}	9.39 ^{+0.07} _{-0.07}	1.8 ^{+0.1} _{-0.1}	10.1 ^{+1.4} _{-1.2}	4.8 ^{+0.3} _{-0.3}
10	9.3 ^{+1.8} _{-1.7}	5.15 ^{+0.01} _{-0.02}	7.0 ^{+0.2} _{-0.2}	22.6 ^{+3.1} _{-3.0}	13.8 ^{+0.8} _{-0.8}	9.36 ^{+0.07} _{-0.07}	1.6 ^{+0.1} _{-0.1}	7.7 ^{+1.3} _{-1.2}	4.2 ^{+0.3} _{-0.3}
11	8.7 ^{+1.3} _{-1.4}	5.13 ^{+0.01} _{-0.01}	6.9 ^{+0.2} _{-0.2}	21.3 ^{+2.2} _{-2.3}	13.5 ^{+0.6} _{-0.6}	9.40 ^{+0.06} _{-0.06}	1.6 ^{+0.1} _{-0.1}	7.2 ^{+0.9} _{-1.0}	4.2 ^{+0.2} _{-0.2}
12	5.7 ^{+1.2} _{-1.0}	5.11 ^{+0.01} _{-0.01}	6.5 ^{+0.1} _{-0.1}	16.2 ^{+2.0} _{-1.8}	12.2 ^{+0.5} _{-0.5}	9.48 ^{+0.04} _{-0.05}	1.5 ^{+0.1} _{-0.1}	5.3 ^{+0.8} _{-0.7}	3.7 ^{+0.2} _{-0.2}
Mean	10.5	5.15	7.1	24.7	14.4	9.42	1.7	8.5	4.5
St.Dev.	5.5	0.05	0.7	9.7	2.6	0.05	0.2	3.7	0.9
A		9.812(-03)	1.339(-01)	1.753(+00)	4.621(-01)	-4.544(-06)	4.046(-04)	6.676(-03)	1.567(-03)
B		5.047(+00)	5.713(+00)	6.185(+00)	9.492(+00)	9.475(-03)	1.249(-02)	1.458(-02)	2.811(-02)

C. Atmospheric approximations and zenith distance dependence

In common observational practice simplifying approximations are introduced at the cost of accuracy. These approximations rely on assumptions that the atmosphere: (i) is composed of a single uniform and isotropic layer, (ii) has a flat geometry and (iii) is optically thin. In the following sections we briefly discuss these assumptions.

1. Single-layer atmosphere

A single layer atmosphere has a single physical temperature T (see Eq. 12) that is often assumed to be somewhere between 250 K and 290 K. However, given the reconstructed atmospheric model it is easy to derive this value.

From Eq. 11 the atmospheric emission of a multi-layer, flat atmosphere with a vertical temperature profile can be written as:

$$I_{\nu, \text{atm}} = B_{\nu}(T_{\text{CMB}})e^{-\tau(z_d)} + \sum_{i=1}^N B_{\nu}(T_i)(1 - e^{-\tau_i(z_d)}), \quad (20)$$

where T_i is the i 'th layer temperature, τ_i is its optical depth, and N is the total number of layers (Sec. III). $I_{\nu, \text{atm}}$ is the calculated atmospheric specific intensity, for which the brightness temperature is given by Eq. 16. and is tabulated along with τ in Tab. III. An obvious consequence of considering a multi-layer atmosphere is that it does not have a single physical temperature, because it is a combination of multiple components, each having a different temperature (Eq. 20).

A multi-layer atmosphere however can be assigned a single-layer atmosphere equivalent temperature, T_{SL} , that yields:

$$I_{\nu, \text{atm}} = B_{\nu}(T_{\text{CMB}})e^{-\tau(z_d)} + B_{\nu}(T_{\text{SL}}(\nu))(1 - e^{-\tau(z_d)}). \quad (21)$$

Combining Eq. 20 and Eq.21 gives

$$T_{\text{SL}}(\nu) = \frac{h\nu}{k_B \ln D}, \quad (22)$$

$$D = \frac{2h\nu^3}{c^2} \frac{1 - e^{-\tau(z_d)}}{I_{\nu, \text{atm}} - B_{\nu}(T_{\text{CMB}})e^{-\tau(z_d)}} + 1.$$

For a single layer atmosphere $N = 1$ and $T_{\text{SL}} = T_1$, and it is frequency independent. In general, however, T_{SL} depends on frequency because at different layers the temperature T_i (Eq. 20) is weighted by coefficients $\sim (1 - e^{-\tau_i})$ that depend on frequency differently than $(1 - e^{-\tau})$ (Eq. 16), and hence the frequency dependence does not cancel. T_{SL} is obviously season dependent too, and it can be readily derived from Eq. 23 using using Eq. 16, T_{atm} and τ estimates from Tab. III. However, in the optically thin limit, T_{SL} is a sensitive function of T_{atm} and τ . T_{SL} is also a weak function of zenith distance. At zenith, in the optically thin limit, it is a combination of all atmospheric layers, but near the horizon the lowermost atmospheric layers begin to dominate all other contributions. Within the flat-atmosphere model, T_{SL} will reach the ground-level atmospheric temperature at the horizon, but it will still vary from one season to another. In the optically thick limit, $T_{\text{SL}} = T_{\text{atm}}$ and it also loses its frequency dependence because in this limit, the geometry is reduced to a single layer case.

In Fig. 11 we plot the calculated T_{SL} temperatures. Individual curves result from the best fit atmospheric models cal-

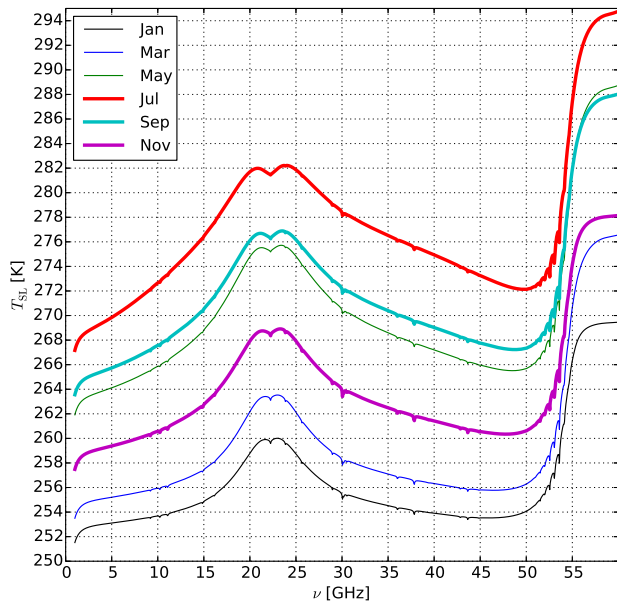


Figure 11: Single-layer atmosphere equivalent temperature resulting from the best fit model obtained from the combined PWV data samples (Tab. II). From the bottom to the top thin lines correspond to January, March and May, and from the top to the bottom thick lines are calculated for July, September and November.

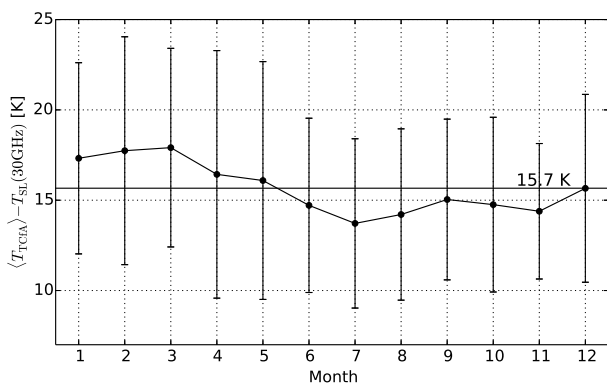


Figure 12: Relationship between the single-layer atmosphere equivalent temperature, T_{SL} , at 30 GHz, at zenith (see Eq. 21) and the ground-level month-median atmospheric temperature at TCfA. The difference between the two is consistent, within $\pm 1\sigma$ error bars, with a constant offset of about 15.7 K. The error bars represent the monthly ground-level temperature dispersion at TCfA. The median and standard deviation of the ground-level atmospheric temperatures are calculated using the meteorological data introduced in Sec. II D.

culated for the selected months. The spectra were calculated using Eq. 23, but due to the strong sensitivity of T_{SL} to τ and T_{atm} the values cannot be constrained to a precision bet-

ter than O(10) K from the current data.¹⁰ The dents coincide with the resonance frequencies of water and ozone lines.

For any given frequency the single-layer atmosphere equivalent temperature (T_{SL}) should be most affected by the physical temperatures of layers that are most responsible for absorption of radiation at that frequency. About 50% of total WV contribution to T_{atm} takes place above altitudes 1-2 km (where the temperature is at least 5-10 K below the ground temperatures). At these altitudes there is also the biggest concentration of WV. Similarly the typical high scale for $\sim 50\%$ of oxygen absorption is about ~ 5 km with typical temperatures ~ 30 K lower than the ground temperatures.¹¹ Since at 30 GHz the contributions to T_{atm} from oxygen and WV are similar, the expected single-layer atmosphere equivalent temperature should be about ~ 20 K lower than the ground temperature. A result of a numerical calculation at 30 GHz is shown in Fig. 12. Clearly, for the location of TCfA a reasonable estimate of T_{SL} , at 30 GHz, can be found from the ground level temperatures, offset by ~ 15.7 K. The offset for other frequencies can be inferred from Fig. 11. Given the sensitivity of T_{SL} (Eq. 21) to τ , the offset ground-level atmospheric temperature may provide a better constraint than measurements of τ and T_{atm} .

As mentioned earlier, T_{SL} also depends on zenith distance, but we find that the dependence is rather weak and for $z_d \leq 89^\circ$ in January (July) the dependence for 30 GHz is constrained by:

$$(T_{\text{SL}}(z_d) - T_{\text{SL}}(0)) \cos(z_d) \lesssim 0.15(0.25) \text{ K} \quad (23)$$

Up to $z_d = 75^\circ$, $T_{\text{SL}}(z_d)$ is roughly constant, and fixed at its zenith value, with accuracy better than $\{0.2, 0.3, 1.5, 0.8\}$ K at frequencies $\nu = \{5, 15, 22, 30\}$ GHz in July. Deviations from the zenith values are even smaller in January.

2. Planar atmosphere

Radio telescopes with Az-El mount cannot efficiently observe sources towards zenith, thus from practical reasons the dependence of T_{atm} on zenith distance (z_d) is important. Based on the Bemporad's air-mass-zenith-distance fitting formula, $A_m(z_d)$, (see Schoenberg (1929) or Wilson et al. (2009)), it can be seen that the assumption of flatness of the atmosphere – i.e. the atmosphere being composed of flat layers stacked one over another – is consistent with $\sec(z_d)$ scaling to within 0.25% (3%) up to $z_d < 60^\circ(80^\circ)$. Within this approximation the atmospheric optical depth is given by

$$\tau(z_d) = \tau(0) \sec(z_d), \quad (24)$$

where $\tau(0) \equiv \tau(z_d = 0^\circ)$. We assess the accuracy of this approximation by means of radiative transfer through atmospheric layers, whose thicknesses are increased to match ray

¹⁰ For example, a variation of τ by 10^{-3} at 30 GHz in July implies a ~ 4 K change in T_{SL} (Tab. III).

¹¹ Rough estimates found using the best fit model in July.

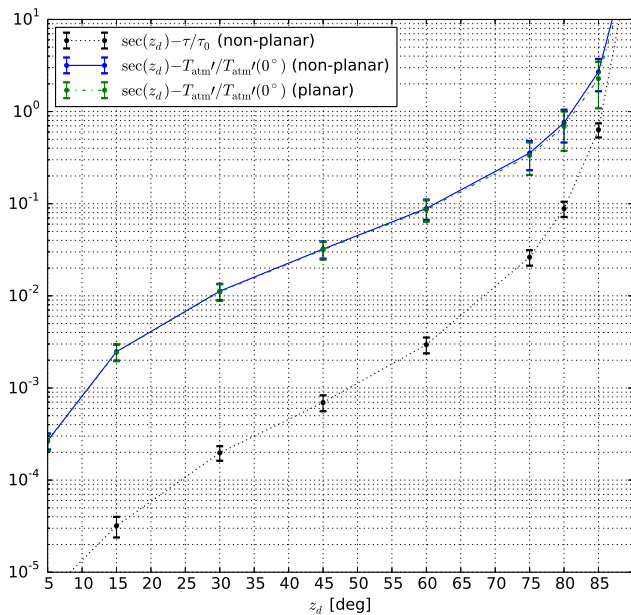


Figure 13: Mean zenith distance dependence of $\tau/\tau(0^\circ)$ (dotted), and $T'_{\text{atm}}(z_d)/T'_{\text{atm}}(0^\circ)$ (solid/dash-dotted) for the best-fit local atmospheric model. Error bars represent $\pm 1\sigma$ deviation about the mean due to frequency and month dependence.

path lengths travelling through spherical layers at given zenith angle. As before, we use the same setup of $N = 300$, layers distributed as discussed in Sec. III, but in this case each layer is assumed to be located between geocentric radii R_i and R_j and hence its thickness $h_{ij} = R_j - R_i$ at the zenith angle z_d (measured from the surface of the Earth), is given by:

$$h_{ij}(z_d) = (R_i^2 + R_j^2 - 2(R_\oplus^2 + C_i C_j) \sin^2(z_d))^{1/2} \quad (25)$$

$$C_i = \sqrt{R_i^2 \csc^2(z_d) - R_\oplus^2}$$

$$C_j = \sqrt{R_j^2 \csc^2(z_d) - R_\oplus^2},$$

where we assumed spherical Earth.

For each month, we use the best-fit atmospheric profile and calculate $\tau(z_d)$ relations for a range of zenith distances, at the frequencies $\nu[\text{GHz}] = \{5, 15, 22, 30\}$. Then we normalise $\tau(z_d)$ at zenith and average between different frequencies and seasons. We will hereafter refer to the resulting relation as air-mass (A_m), because in the limit of flat atmosphere its behaviour follows that, expected from the air-mass relation defined as a zenith-normalised ray path length, with $A_m(60^\circ) = 2$ and A_m assuming infinity at the horizon. The differences between individual months (January and July) and frequencies vary between 40 and 53 air-masses at the horizon, and between 30 and 35 air-masses at $z_d = 89^\circ$, and between 10.6 and 11 air masses at $z_d = 85^\circ$.

The following fourth order in $\sec(z_d)$ fitting function provides a good fit to the reconstructed relation, with the maximal

deviation below 0.3% at $z_d = 89^\circ$:

$$A_m(z_d) = 1.00 \sec(z_d) - 3.74 \cdot 10^{-4} \sec^2(z_d) \quad (26)$$

$$- 4.67 \cdot 10^{-4} \sec^3(z_d) + 6.04 \cdot 10^{-6} \sec^4(z_d).$$

We do not use $z_d = 90^\circ$ data point to avoid singularity but since the effects of refraction are not taken into account, the usability of the formula is effectively reduced down to $z_d \lesssim 85^\circ$, where the dispersion due to season and frequency dependence becomes similar to uncertainties due to neglected refraction. Given the vertical profiles of temperature and humidity, it is straightforward to implement refraction corrections, but since the lowest elevations are uninteresting from practical reasons, we defer this improvement to possible future work.

According to the fitting formula, the assumption of the flat atmosphere (Eq. 24) is accurate to within 0.16 (1.6%) at $z_d = 60^\circ$ (80°), where the air mass is 1.997 ± 0.001 (5.670 ± 0.025) and where the error bars represent the 1σ dispersion due to season and frequency dependence.

To address the problem described at the beginning of this section, we calculate the average $\tau/\tau(0^\circ)$, and $T'_{\text{atm}}(z_d)/T'_{\text{atm}}(0^\circ)$ relations for the planar and non-planar atmospheres (Fig. 13). This is useful because radio telescopes are directly sensitive to increases of antenna temperature. The relations are derived according to the best fit atmospheric model (last column of Tab. II). The $\tau/\tau(0^\circ)$ relation for the planar case is given by $\sec(z_d)$ and is not plotted. As will be discussed in Sec. IV C 3, T'_{atm} is the atmospheric brightness temperature calculated for the case when the CMB is not present as a source term in the radiative transfer equation, hence $T_{\text{atm}} \approx T'_{\text{atm}} + T_{\text{CMB}}$. Clearly, the average deviation of T'_{atm} from the $\sec(z_d)$ scaling is ≈ 0.1 (0.4) or alternatively: $(\sec(z_d) - T'_{\text{atm}})/\sec(z_d) \approx 5\%$ (10%) at $z_d = 60^\circ$ (75°). The effects due to planarity are more than order of magnitude smaller. The difference between the averaged $\tau/\tau(0^\circ)$ and $T'_{\text{atm}}/T'_{\text{atm}}(0^\circ)$ scalings increases as the optical depth escapes beyond the optically thin limit. This is discussed in the next section.

3. Optically thin atmosphere

Within the RJ approximation $B_\nu(T) = 2\nu^2 k_B T / c^2$, and Eq. 20 becomes:

$$T_{\text{atm}}(z_d) = T_{\text{CMB}} e^{-\tau(z_d)} + \sum_{i=1}^N T_i (1 - e^{-\tau_i(z_d)}). \quad (27)$$

The approximation of optically thin atmosphere is often exploited by utilising the first order expansion in τ

$$T_{\text{atm}}^{(1)}(z_d) = T_{\text{CMB}}(1 - \tau(z_d)) + T_{\text{SL}}\tau(z_d), \quad (28)$$

where, as before, we utilised the single layer equivalent temperature at zenith (see below). We checked that in order to

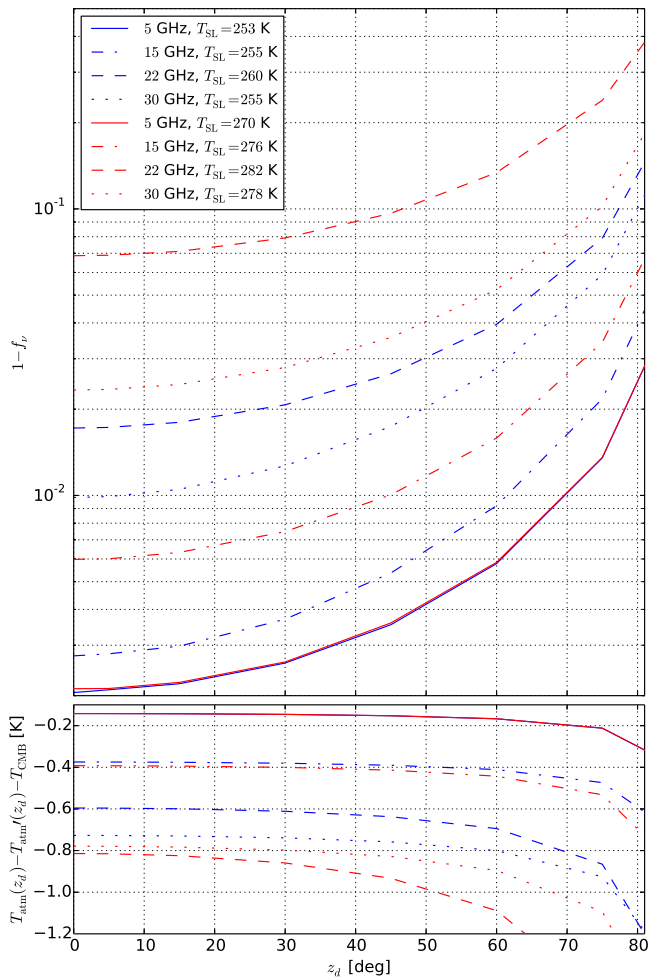


Figure 14: (*Top panel*) Accuracy of the atmospheric brightness temperature linear order expansion (Eq. 31) in January (blue) and July (red). The best-fit model ($p_H = 0.62$) from the combined PWV data samples (Tab. II) is used. For each frequency the zenith T_{SL} values are provided in the plot legend. (*Bottom panel*) Accuracy of $T_{\text{atm}} \approx T_{\text{atm}}' + T_{\text{CMB}}$ approximation expressed as a difference between the actual T_{atm} and the sum of constituents considered separately: T_{CMB} and atmospheric brightness temperature derived without the CMB as a source term (T_{atm}'). [See the electronic edition of the Journal for a colour version of this figure.]

visualise the shortcomings of using the optically thin atmosphere approximation the differences due to introducing the RJ approximation are unimportant.

Depending on what is being measured, T_{CMB} contribution is sometimes treated independently from T_{atm} , as if the CMB was not processed by the altitude dependent absorption. Below, we quantify this approximation, but in general, since the CMB propagates through an absorbing and emitting medium, the two contributions (one from the atmosphere and the other from the CMB) cannot be treated separately. For this reason our constraints on T_{atm} include the CMB as a source term in Eq. 10. Neglecting the CMB as a source term, Eq. 28 for the

case of flat atmosphere (Eq. 24) becomes:

$$T_{\text{atm}}^{(1)}(z_d) = T_{\text{SL}}\tau(0) \sec(z_d), \quad (29)$$

and what follows is that for a single layer atmosphere

$$T_{\text{atm}}'(60^\circ) = 2T_{\text{atm}}'(0^\circ), \quad (30)$$

where $T_{\text{atm}}'(z_d)$ is the atmospheric brightness temperature for $T_{\text{CMB}} = 0$ K. This approximation is often used in tipping scan measurements.

Increasing the air mass, by looking at larger z_d angles, the linear-order approximation in Eq. 29 must fail at large values of τ as T_{atm} (or T_{atm}') cannot reach infinity. The ratio of Eq. 27 and Eq. 28:

$$f_\nu(T_{\text{CMB}}, T_{\text{SL}}, \tau_0, z_d) = T_{\text{atm}}/T_{\text{atm}}^{(1)} \quad (31)$$

gives a factor by which T_{atm} is underestimated by using the linear-order single-layer approximation. Notice that Eq. 28, and consequently Eq. 29, introduce yet another, commonly used approximation, that T_{SL} does not depend on z_d , but instead is fixed at its zenith value. As discussed in Sec. IV C 1, this is a quite reasonable approximation for a range of z_d s. T_{atm} in Eq. 31 is calculated numerically within the flat atmosphere approximation, and $T_{\text{atm}}^{(1)}$ is calculated according to Eq. 28 with $\tau(z_d)$ derived numerically and with T_{SL} calculated from Eq. 23.

The factor f_ν depends on τ , frequency, and vertical temperature profile of the atmosphere. Assuming a flat and single-layer atmosphere without the CMB, it is easy to see that the factor becomes independent of atmospheric temperature and at $z_d = 60^\circ$ amounts to $f(T_{\text{CMB}} = 0 \text{ K}, \tau_0) = (1 - e^{-\tau_0 \sec(z_d)})/(\tau_0 \sec(z_d)) \approx 0.965(0.94)$ at 30 GHz for the best-fit value of $\tau_0 = 0.036(0.061)$ in January (July) (Tab. IV).

The zenith distance dependence of f_ν is shown in Fig. 14 (top panel). The difference between various line styles within the same colour results from the frequency dependence. Comparing lines within the same line style gives the hot/cold season dependence. The single-layer atmosphere equivalent temperature at zenith is given in the plot legend. The bias is strongly frequency dependent. It is largest around 22 GHz, and in July it reaches $\sim 13\%$ at $z_d = 60^\circ$. At 30 GHz and for the same zenith distance the bias is between $\sim 3\%$ and $\sim 5\%$ depending on the season, in rough agreement with the single layer atmosphere estimates (see above).

In the bottom panel of Fig. 14 errors of considering T_{CMB} independently from T_{atm} are quantified. These are lowest at low frequencies, small optical depths and zenith angles (see plot description for details).

4. Relation to observations

The approximations discussed in the previous sections may affect the radio source flux density observations at the levels of few to several per-cent.

In particular, estimates of the atmospheric absorption corrections may be biased depending on the assumed approximations. Flux-density absorption corrections within the flat and optically thin atmosphere model are given by:

$$S_t = S_m e^{\tau_0 \sec(z_d)} \approx S_m (1 + \tau_0 \sec(z_d)) \quad (32)$$

where S_t is the true flux density and S_m is the measured flux density. These corrections require an estimate of $\tau = \tau(\nu, z_d, m)$, which is a function of frequency (ν), zenith distance (z_d), and month (m).

With a single-dish radiometers τ is typically estimated by measuring the system temperature components at zenith and at $z_d = 60^\circ$ with an implicit assumption of the validity of Eq. 30. In the simplest case, when detector linearity is assumed and the spillover, side-lobe and ground pick-up contributions are neglected, in the RJ approximation, the measurement can be defined by the following system of linear equations:

$$\begin{aligned} c_f V(0^\circ) &= T'_{\text{atm}}(0^\circ) + T_{\text{rx}} + T_{\text{CMB}} + \Delta T_\nu(0^\circ) \\ c_f V(60^\circ) &= A_m(60^\circ) T'_{\text{atm}}(0^\circ) + T_{\text{rx}} + T_{\text{CMB}} + \Delta T_\nu(60^\circ) \\ c_f V_{\text{abs}} &= T_{\text{abs}} + T_{\text{rx}}, \end{aligned} \quad (33)$$

where T_{rx} is the receiver noise temperature, T_{abs} is the absorber temperature and c_f is a conversion factor from the voltage, measured at the square-law detector, to the units of antenna temperature, and $V(z_d)$ is the measured voltage at z_d . Here, we used T'_{atm} to separate out the offset due to CMB (T_{CMB}). ΔT_ν is a correction factor weakly dependent on zenith distance (Fig.14 bottom panel). Usually, at $z_d = 60^\circ$ the $A_m = 2$ (and $\Delta T_\nu = 0$) is assumed, in accord with the flat atmosphere expectation.

Substituting thus derived value of T'_{atm} into Eq. 29 with an assumed value of T_{SL} gives an estimate of τ . This is a possible source of systematical effects. First, as discussed in Sec. IV C 1, T_{SL} follows ground level temperatures and fixing its value will lead to season dependent systematical effects. Secondly, Fig. 14 indicates that using approximation of Eq. 29 leads to a slight, but systematical underestimation of τ and S_t . In practice, absorption corrections are applied to both, the target source at z_d^{src} and the chosen flux calibrator at the zenith distance z_d^{cal} , hence the effects of the approximation in Eq. 30 on the relative flux density will cancel, as long as the calibrator and the target source happen to be observed at the same z_d . This is however almost never the case, and so the effects of the approximation will propagate onto the flux density estimates through factors $\sim (1 + \tau_0 \sec(z_d^{\text{src}}))/(1 + \tau_0 \sec(z_d^{\text{cal}}))$. Since the calibrator and target sources are observed at different elevations, this effectively leads to an increased variance of flux density estimates for individual sources, disparities between sources of the same intrinsic flux density, and possibly to systematical effects depending on source declination with respect to the calibrator.

D. Altitude dependence

The impact of the observation site altitude on the atmospheric emissions is significant (Fig. 15). Increasing observa-

tion site altitude leads to: (i) decreasing Doppler and pressure line broadening and (ii) decreasing zenith air mass and column PWV. This reveals weak and narrow, spontaneously-excited, stimulated emission lines, as T_{atm} and t_{atm} decreases. The flat shape of the oxygen emission in the right-hand side of the plot indicates the line saturation. Clearly, outside of the troposphere the season dependence is very weak.

E. T_{atm}/τ -PWV scaling relation

In the clear sky conditions and for a given vertical profile of PWV, there is 1:1 relation between the measured PWV and T_{atm} . In this section we derive T_{atm} -PWV and τ -PWV scaling relations for January and July, using the best fit model estimate from the combined data samples (Tab. II). In each of the two vertical profiles the PWV content is scaled at all altitudes by constant factors, and the corresponding T_{atm} and τ are recorded. We calculate the scaling relations at frequencies 5,15,22 and 30 GHz and find that the following third order polynomial provides a good fit with negligible residues:

$$X = \sum_{i=0}^3 x_i \left(\frac{w}{1 \text{ mm}} \right)^i \quad (34)$$

where $X = \{T_{\text{atm}}, \tau\}$ and $x_i = \{a_i, b_i\}$. The a_i and b_i coefficients are summarised in Tab. IV. Terms beyond the linear order describe the subtle effects of pressure line broadening and self-induced water vapour continuum absorption, both non-linearly dependent on H_2O VMR (Paine 2015). For τ the scaling is quadratic and so we use the second order polynomial.

In Fig. 16 we visualise T_{atm} scaling relations and the residual errors between these relations and their fitting formulas (Eq. 34). The initial best-fit models, from which the scaling was derived, include the CMB as a source term (Sec. III).

T_{atm} -PWV scaling relation can be used to estimate T_{atm} instabilities due to time varying column PWV. The amplitude of temporal fluctuations of the column PWV, under the frozen turbulence hypothesis, should constrain the spatial power spectrum of water vapour distribution at the scales L , roughly corresponding to $v_w \Delta t$, where Δt is the time interval between subsequent PWV measurements, and v_w is the wind speed at relevant altitudes. Alternatively, under the same assumptions, two instantaneous measurements of PWV, performed at two locations separated by distance L , probe the turbulent spectrum of PWV at the scales roughly corresponding to the spatial separation of the observing sites. While the spectrum of the atmospheric PWV fluctuations is beyond the scope of this paper, we provide a rough estimate of the amplitude of the T_{atm} variations in the clear sky conditions, based on the Sun photometer measurements of the column PWV.

Since the T_{atm} -PWV scaling relation is dominated by the linear terms (a_0 and a_1) the a_1 term can be thought of as an approximation of the derivative $\frac{dT_{\text{atm}}}{dw}$ which quantifies T_{atm} response to variations in PWV (w). Tab. IV shows that PWV variation of ~ 0.2 mm (~ 0.3 mm) would cause T_{atm} variation of the order $\Delta T_{\text{atm}} \approx 0.09$ (0.14) K at 30 GHz in

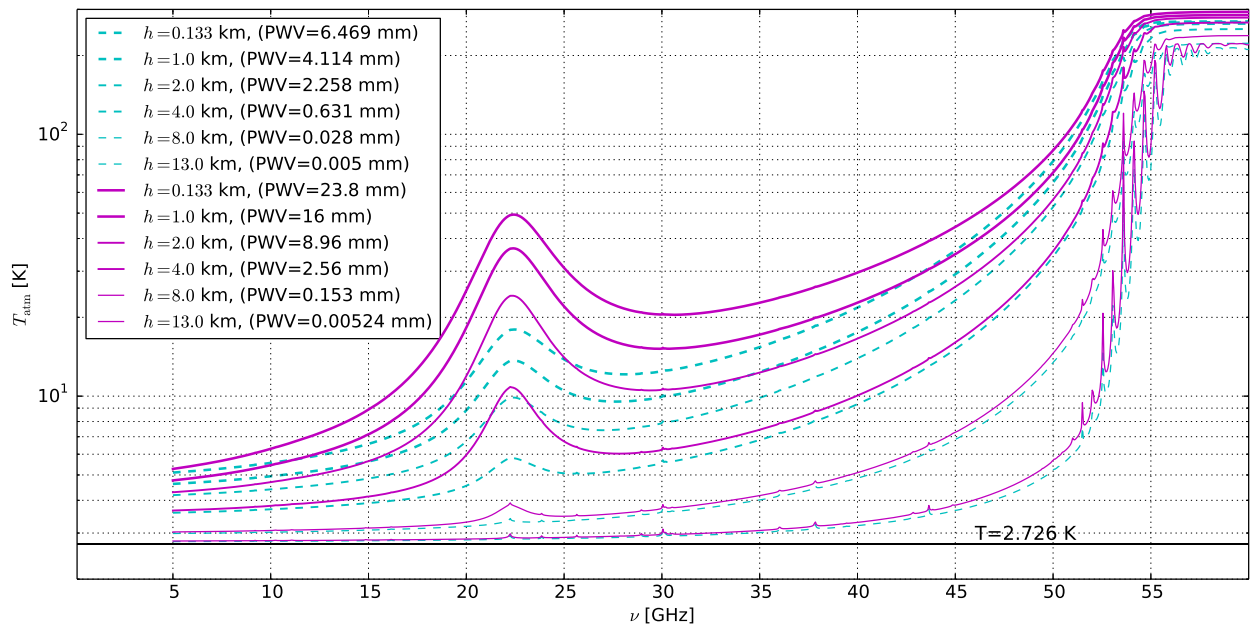


Figure 15: Atmospheric brightness temperature altitude dependence in January (dashed, cyan) and July (solid, magenta) for $p_H = 1.0$. The horizontal line marks the temperature of the CMB.

Table IV: T_{atm} -PWV and τ -PWV fitting formula coefficients (Eq. 34). The numbers are written in scientific notation with the decimal exponent in parentheses. The “error” column contains standard deviations of the difference between the derived scaling and the corresponding fitting formula.

ν [GHz]	January								
	a_0 [K]	a_1 [K/mm]	a_2 [K/mm ²]	a_3 [K/mm ³]	error [mK]	b_0	b_1 [mm ⁻¹]	b_2 [mm ⁻²]	
5	5.055(+00)	8.104(-03)	7.997(-05)	-2.841(-09)	2.441(-06)	9.350(-03)	3.108(-05)	3.047(-07)	
15	5.738(+00)	1.282(-01)	6.849(-04)	-3.392(-07)	2.551(-04)	1.209(-02)	4.921(-04)	2.741(-06)	
22	6.833(+00)	1.644(+00)	-3.827(-03)	8.033(-06)	1.434(-01)	1.650(-02)	6.391(-03)	5.896(-06)	
30	9.477(+00)	4.603(-01)	2.396(-03)	-4.450(-06)	6.191(-03)	2.729(-02)	1.792(-03)	1.096(-05)	
July									
5	5.062(+00)	7.640(-03)	5.368(-05)	-2.070(-09)	3.662(-04)	8.820(-03)	2.728(-05)	1.901(-07)	
15	5.705(+00)	1.245(-01)	4.551(-04)	-2.370(-07)	3.417(-02)	1.125(-02)	4.450(-04)	1.710(-06)	
22	6.739(+00)	1.825(+00)	-4.879(-03)	6.163(-06)	9.216(-01)	1.515(-02)	6.616(-03)	3.679(-06)	
30	9.230(+00)	4.455(-01)	1.555(-03)	-3.130(-06)	3.457(-01)	2.472(-02)	1.612(-03)	6.840(-06)	

January (July). These are the amplitudes of the PWV variations in the clear sky conditions we actually observe at ~ 1 -hour time scales.¹² Clearly, low column PWV values also result in a stabler atmospheric brightness temperature. By the Kolmogorov’s atmospheric turbulence model, the brightness fluctuations are characterised by a steep spectrum over a wide range of spatial frequencies, and the overall variance is dominated by the largest scales. For the wind speed of the order $O(1)$ m/s typical for the calm sky without frontal activities, 1-hour time scale corresponds to $L \sim O(10)$ km length scales, which coincide with the largest scales from

the inertial sub-range, in which the atmospheric turbulence driven cascade of kinetic energy transport takes place. Incidentally, this rough estimate remains in agreement with theoretical predictions from the atmospheric turbulence model (Baars 2007), which for the same frequency, at the sea level gives $\Delta T_{\text{atm}} \approx 0.0055 T_{\text{atm}}$, that is $\Delta T_{\text{atm}} \approx \{0.06, 0.11\}$ K for January and July respectively (Tab. III). This is also qualitatively compatible with an independent analysis involving the near-ground RH variability and wind speed measurements (Lew 2016, in preparation).

F. Accuracy limits

The uncertainties of the local, mean T_{atm} and τ range from $\sim 0.2\%$ at 5 GHz to $\sim 13\%$ at 22 GHz (see Tab. III for January). These uncertainties refer to the monthly mean esti-

¹² The amplitude of the PWV variations quoted are examples from a single day observations in January and July, but the amplitude depends on the considered time-scale, and also somewhat varies from one day to another.

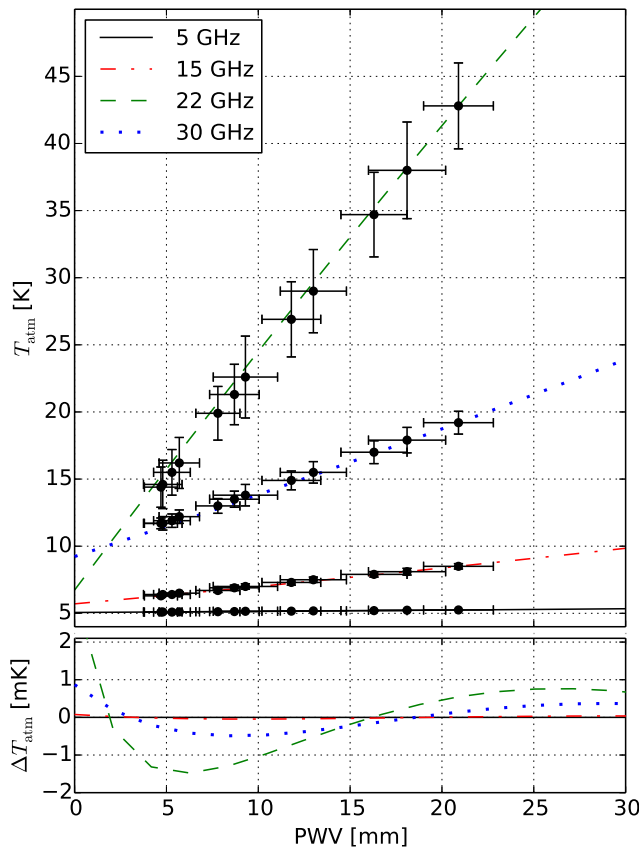


Figure 16: (*top panel*) T_{atm} -PWV scaling relations given by Eq. 34 and Tab. IV (lines). The four sets of points over each of the lines represent the best-fit model brightness temperatures from Tab. III. (*bottom panel*) Residues between the calculated scaling relations described in Sec. IV E, and their respective fitting functions.

mates, rather than to individual PWV measurements, although the dispersion of the individual measurements affects the χ^2 value when model fitting. A random PWV measurement may deviate significantly from the mean even in the clear sky conditions (e.g. see the scatter from individual PWV measurements in Fig. 8 or Tab. I). In order to assess accuracy with which the actual T_{atm} and τ can be constrained from the statistical analysis of the climatology data, we calculate the impact of the largest variations, observed in our PWV measurements, on the values of T_{atm} and τ .

The largest observed variation of PWV in our sample occurs in June (Tab. I) and ranges from $w \sim 9$ mm to $w \sim 23$ mm and the 1σ variation is approximately ± 6.1 mm. Assuming linearity of the PWV- T_{atm} relation (a_1 coefficients for July in Tab. IV), this translates to 1σ temperature variations $\Delta T_{\text{atm}} \lesssim \pm\{0.05, 0.8, 11, 2.7\}$ K at $\nu = \{5, 15, 22, 30\}$ GHz, or by about $\Delta T_{\text{atm}}/T_{\text{atm}} \approx \pm\{1, 9, 26, 14\}$ % (see Tab. III for July). Clearly, low frequencies are least sensitive to WV variations.

The fitting formulas defined in Eq. 34 were derived using the best-fit models for January and July by scaling the WV content, hence the T_{atm} (or τ) predicted by these formulas will

not exactly match the best-fit model values from Tab. III. This is because the vertical structure of the atmosphere is month dependent. In order to visualise the amplitude of these differences, for each frequency, we over-plot the twelve T_{atm} values from Tab. III atop the fitting relation obtained for July (Fig. 16). T_{atm} from different months are consistent within 1σ error bars quoted in Tab. III, but a better consistency is reached at high PWV levels, typical for summer months, as expected. The year-average PWV- T_{atm} scalings, which result from fitting the data points from Fig. 16, are given by A and B coefficients in Tab. III.

G. Clear sky detection

By the analysis of the ground-level solar irradiance (E_{\odot}), temperature (T) and all-sky images, we observe that in the clear sky conditions there is a good positive correlation between the solar irradiance and air temperature. At such times E_{\odot} and T are smooth functions of time. On the other hand, clouds passing through the LOS towards the Sun generate a high frequency noise (Fig. 17 second top panels). We anticipate this feature can be used for automatic clouds detection in the analyses of meteorological data, but we defer details to a separate study.

In Sec. I we mentioned that at a fixed pressure level the RH has a diurnal variation corresponding to temperature variations of the atmospheric layer. The RH variation anticorrelates with the near-ground atmospheric temperature and also with the solar irradiance (Fig. 17) detected at DMC. However, IGRA data from Legionowo (Sec. II B 1) are recorded only twice a day (midday and midnight) and it is impossible to analyse the stability of diurnal variations of RH in order to infer the cloud cover. It is therefore, interesting to see how feasible it is to select sub-samples of IGRA data, that would statistically correspond to clear sky conditions, given only few observational parameters: T, P and T_{dew} . We will investigate this using local sky images archived at DMC and T, P and RH measurements from TCfA, coarse averaged at 1-hour time scale. The distance between the two sites is ~ 8 km.

The amplitude of diurnal temperature variations is largest, in clear sky conditions. This is because the radiative cooling of the surface of the Earth is more efficient without the heat-trapping clouds. Since the RH follows these variabilities in anti-phase, it should be expected that at fixed temperatures a selection based on the lowest daytime RH values should statistically correspond to clear sky conditions. On the other hand, thick cloud cover tends to mitigate the amplitude of day to night variations in temperature and humidity. In this section we report results of a statistical analysis aimed to verify the accuracy of this hypothesis.

The hourly averaged ground-level meteorological data (Sec. II D) are screened by RH to form a sub-sample of the 5% driest conditions (sec. II D). In order to mitigate effects of diurnal temperature variations we consider only the samples between hours 10:00 and 14:00 of the UTC+1 time. Such a choice roughly corresponds to the times when the temperatures should be stablest (Fig. 17). The selection typically picks

Table V: Summary of the sensitivity of the cloud detection algorithm by low ground-level RH values for the two cloud cover categories: “All” where all types of clouds are considered, and “Low and Medium” for which high clouds are treated as clear sky.

Cloud cover sky fraction (CI ^c)	Clouds ^a : Season ^b :	True-Positive fraction					
		All [%]			Low & Medium [%]		
		C&H	C	H	C&H	C	H
≤ 0.125 (≤ 1)		24	23	24	57	56	58
≤ 0.250 (≤ 2)		34	29	40	65	56	74
≤ 0.375 (≤ 3)		48	35	62	76	62	89

^aType of clouds considered. “Low & Medium” means that all high clouds (if present) were treated as clear sky.

^b‘H’ - hot season: months from April to September, ‘C’ - cold season: months from October to March, ‘C&H’ - all year.

^cCI - cloud cover index ranging from 0 to 8. For example, CI = 1 corresponds to cloud cover sky fraction of $1/8 = 0.125$.

out two days per each month, condition to data completeness. Next, we visually analyse the all-sky images for the selected days and times and assign a mean cloud cover index for two cases: (i) disregarding distinction between high, medium and low clouds, and (ii) ignoring high clouds i.e. treating them as clear sky. The cloud cover index (CI) is allowed to range from 0 for no clouds situation, up to 8 for the full sky cloud cover. We disregard whether the cloud cover is thin or thick. The result is summarised in Tab. V

Clearly, the selection by RH at the ground level has a high false-positive (low true-positive) fraction when all types of clouds are considered (see “All” column in Tab. V). However the situation significantly improves when high clouds are treated as clear sky. This result is easy to interpret. There is generally a poor correlation between RHs (or the corresponding H₂O VMRs) at different pressure levels (altitudes) hence, there is no guarantee that selection by low near-ground RHs will pick out days with no or little high cloud cover. Even the straightest selection by RH (5% driest days per month) not always select the fully cloudless days. This typically happens for the months during which the sky is cloudy most of the time (such as November in Poland). An example of a false-positive detection is shown in Fig. 17. The two dates were selected by the algorithm. The RH variabilities (bottom panels) and their lowest values are similar in both cases. Yet, the visual inspection revealed that the earlier day was contaminated by high clouds and classified as CI = 6 on the average, as opposed to the latter day classified with CI = 0. It seems however, that solar irradiance measured directly to the Sun could be effectively used to detect clouds by analysing the high frequency Fourier modes of the time domain signal.¹³ When treating high clouds as clear sky, however, the selection of days with cloud cover below 0.375 is accurate in $\sim 76\%$ of cases year-round and in $\sim 89\%$ of cases during hot season (see Tab. V). We have not investigated the specificity of the

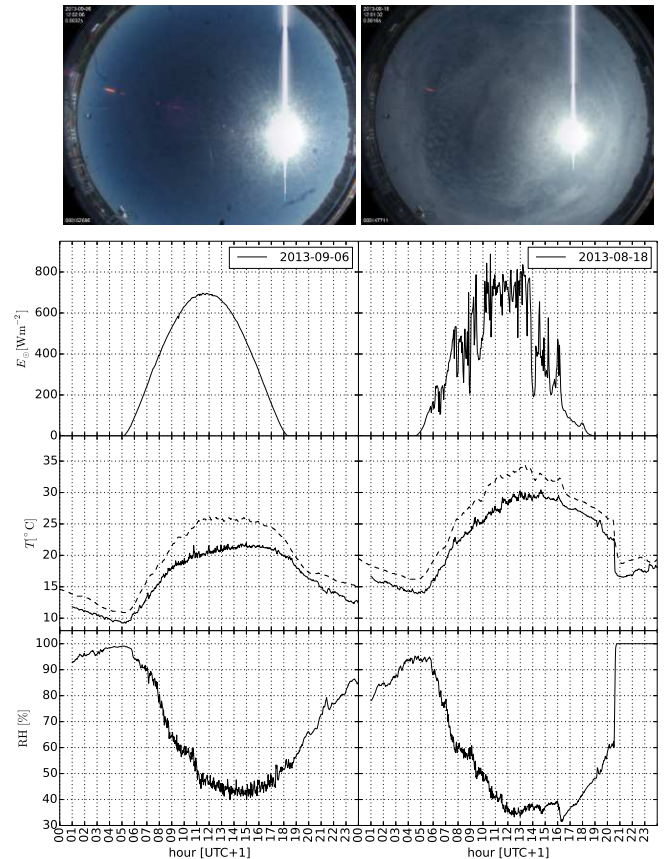


Figure 17: Comparison of atmospheric parameters at two different days identified as clear sky, based on selection by low values of RH. The left panels show the correct selection (with an average 4-hour cloud cover CI = 0), and the right panels show an example of a false-positive selection (with an average 4-hour cloud cover CI \approx 6). From the top to the bottom the panels show the all-sky camera picture around noon (UTC+1), ground-level all-sky solar irradiance, temperature and RH. The dashed lines trace the *CMP 22* pyranometer sensor temperature. While the false-positive selection occurred most likely due to the little impact of high clouds on the near-ground RH, the impact of such a thin layer of high clouds is clearly significant on the detected irradiance.

estimator – i.e. we have not estimated the fraction of clear sky days that eluded detection, but we are aware of such cases.

On the average, disregarding the cloud type, the fraction of days with cloud cover $\leq 20\%$ is $\sim 10\%$ year-round, $\sim 12\%$ in the hot season¹⁴ and $\sim 8\%$ in the cold season for the RT32 region (Woś 2010). Based on the data from Tab. V (interpolated for the cloud cover $\leq 20\%$), in the case of all types of clouds, using a binomial distribution with the number of trials fixed by the number of clear sky day candidates selected by the algorithm, we estimate that the probability of obtaining the reported true-positive rates by chance is very low, $< 10^{-4}$.

¹³ We measure the solar irradiance using the *CMP22* pyranometer operating in the spectral range from 200 nm to 3600 nm and within $\sim 180^\circ$ FOV.

¹⁴ See Tab. V for the definitions of the hot and cold seasons.

Here, we assumed a true-positive outcome as a successful trial, with the probability defined by the aforementioned cloud cover statistics established by the local climate.

While the algorithm selecting clear sky conditions by low, ground-level RHs yields a statistically significant result, we have not investigated the true-positive fractions when only a single measurement per day is available (case for IGRA data). It's possible however, that the algorithm can be improved, by modifying the time range for data selection (here set between 10:00 and 14:00 of UTC+1), or by altering the RH threshold (here set at 5% of driest conditions), or by including the long-term pressure variations. Due to the reasons described in Sec. II E, for the main analysis, we employed external PWV measurements to match the data selection criteria to the clear sky requirements.

V. DISCUSSION

A comparison of the CIRA86 and Legionowo radiosonde data in terms of temperature shows that the measurements agree very well in the region of the upper troposphere (Fig. 3). However, it has been shown, that there exist a systematical dependence of radiosonde RHs on geographical location, resulting from the instrumentation that was typically used in Eastern/Central Europe, China and the former Soviet Union, and that typically used in the West (Soden & Lanzante 1996). The earlier, exploiting the goldbeater's skin humidity sensors, systematically measure the upper troposphere moisture by about 15% - 20% relative to satellites and capacitive or carbon hygistor sensors (used in the West). Soden & Lanzante (1996) found this systematical effect using the radiosonde data from years 1979-1991. For this reason, in this analysis we refrain from using data from the previous century and rely on the data from the previous and current decades (as it is likely that technology exchange have mitigated these inconsistencies). Peixoto & Oort (1996) has also investigated radiosonde humidity data (recorded in the period from 1973 to 1988), performed cross-checks with SAGE satellite measurements, and found similar discrepancies as those pointed out by Soden & Lanzante (1996), but also confirmed that in the lower and middle troposphere the discrepancies are not important.

VI. CONCLUSIONS

We use climatological data to reconstruct the vertical structure of the atmosphere, constrain month-dependent profiles of precipitable water vapour (PWV), and predict the atmospheric brightness temperature (T_{atm}) and optical depth (τ) at cm-wavelengths. We demonstrate that nearly global coverage of the publicly available climatological data allows to investigate almost every location world wide, with the spatial resolution of few hundred kilometres, on the average (Sec. II).

We compare the month-dependence of the column PWV, reconstructed for the location of the 32-metre radio telescope (RT32), located near Toruń (Poland), with the AERONET

data, collected at the closest station located in Belsk. We find that the two are closely correlated throughout the year, which supports the reliability of the PWV reconstruction from sounding and ground-base meteorological data.

Bearing in mind prerequisites of radio source continuum flux density measurements at cm-wavelengths, we focus at radiative properties of the atmosphere in clear sky conditions. We present a compilation of ~ 17 months of local PWV observations collected in the clear sky conditions using the MICROTOS II Sun photometer (Sec. IV A). We use these observations to devise a selection criterion, which when applied for the climatological data, allows to reconstruct the vertical structure of the atmosphere compatible with a cloudless sky.

Using the reconstructed clear sky PWV profile, and solutions of the radiative transfer through the atmosphere, we constrain T_{atm} and τ for the first time for the location of RT32 (Sec. IV B). We also establish PWV- T_{atm} and PWV- τ scaling relations (Sec. IV E) that can be used to constrain atmospheric brightness temperature and optical depth in the clear sky conditions, given an independent estimate of PWV (e.g. from a local GPS station). We estimate that in the clear sky conditions, the the mean monthly values of T_{atm} and τ , inferred from climatology data, constrain the actual values to within $\pm\{1, 9, 26, 14\}$ % (at 1σ CL) at $\nu = \{5, 15, 22, 30\}$ GHz. These estimates should also apply for other locations at similar latitudes and a compatible climate (Sec. IV F).

We calculate zenith distance (z_d) dependence of T_{atm} and discuss $\lesssim 10\%$ effects regarding radio-source continuum flux density measurement calibrations. We discuss the implications of using optically thin, single-layer, flat atmosphere approximations in determining the optical depth and estimating corrections for atmospheric absorption (Sec. IV C 4). For the selected frequencies, we quantify deviations of $T_{\text{atm}}(z_d)$ function from a simple geometrical scaling $\sim \sec(z_d)$, and calculate air-mass-zenith-distance relation for non-planar atmosphere. We also constrain the physical temperature of the multi-layer atmosphere by introducing a single-layer equivalent temperature, which we next connect to the ground level temperatures by a simple relation (Sec. IV C). The connection should be readily useful when constraining atmospheric optical depth due to absorption and scattering.

Finally, we discuss a clear sky selection criterion involving the ground-level relative humidity (RH). This criterion can be used to detect cloudless days from data that only contain measurements of a few basic atmospheric parameters, such as temperature, pressure and dew point, which are typically collected by weather balloons and ground meteorological stations. By the analysis of archival all-sky images, we find that for any given month selecting meteorological data by lowest daytime RH can correctly identify days with mean cloud cover below ~ 0.38 in 48% of cases, if one disregards whether the sky is obscured by low, medium or high level clouds, and in 76% of cases if only low and medium level clouds are considered. We find that reproducing these true-positive fractions by chance is unlikely at odds greater than $10^4 : 1$ taking into account the local probability of cloudless skies, and the number of days used for the analysis (Sec. IV G). We find that the effectiveness of the estimator is increased during the hot sea-

son (April–September) when the true-positive fraction among the clear-sky days selected by this algorithm reaches $\sim 89\%$ (for the case when high level clouds are treated as clear sky). We suspect that the effectiveness of this estimator should be similar in other locations with a compatible climate.

Acknowledgements

BL would like to thank Mike Peel and Marcin Gawroński for useful discussions on observational pipelines used in OCRA observations. Also thanks to Scott Paine for comments on PWV- τ scaling relations. Thank you to Peter Wilkinson for comments on the early version of the manuscript and to Boud Roukema for comments and suggestions.

Use was made of the data from the Global Climatology of Atmospheric Parameters from the Committee on Space Research (COSPAR) International Reference Atmo-

sphere (CIRA-86) Project. We acknowledge the use of Integrated Global Radiosonde Archive (IGRA) data from Legionowo station. Use was made of the data provided by the Canadian Atmospheric Chemistry Experiment. We thank Piotr Sobolewski, Brent Holben and Aleksander Pietruczuk for their effort in establishing and maintaining Belsk AERONET station.

This work was financially supported by the Polish National Science Centre through grant DEC-2011/03/D/ST9/03373. A part of this project benefited from the EC RadioNet FP7 Joint Research Activity “APRICOT” (All Purpose Radio Imaging Cameras On Telescopes). Use was made of the AM program (version 7.2) – a publicly-available tool for radiative transfer computations at microwave to submillimeter wavelengths, developed at the Harvard-Smithsonian Center for Astrophysics. Use was made of the “matplotlib” plotting library (Hunter 2007) distributed on the GPL-compatible Python Software Foundation license.

-
- Ajello, C., Bonelli, G., & Sironi, G. 1995, *ApJS*, 96, 643
 Akima, H. 1970, *JACM*, 17, 589
 Alduchov, O. & Eskridge, R. 1997, *J. Appl. Meteor.*, 35, 601
 Baars, J. W. M. 2007, *The Paraboloidal Reflector Antenna In Radio Astronomy And Communication Theory And Practice* (Springer New York)
 Bernath, P. F., McElroy, C. T., Abrams, M. C., et al. 2005, *Geophys. Res. Lett.*, 32, L15S01
 Bussmann, R. S., Holzappel, W. L., & Kuo, C. L. 2005, *ApJ*, 622, 1343, [astro-ph/0412031]
 Bustos, R., Rubio, M., Otárola, A., & Nagar, N. 2014, *PASP*, 126, 1126, [1410.2451]
 Carleer, M. R., Boone, C. D., Walker, K. A., et al. 2008, *Atmospheric Chemistry and Physics Discussions*, 8, 4499, 00035
 Durre, I., Vose, R. S., & Wuertz, D. B. 2006, *J. Climate*, 19, 53
 Fioletov, V. E., Bodeker, G. E., Miller, A. J., McPeters, R. D., & Stolarski, R. 2002, *J. Geophys. Res.*, 107, 4647
 Fixsen, D. J. 2009, *ApJ*, 707, 916, [0911.1955]
 Gawroński, M. P., Peel, M. W., Lancaster, K., et al. 2010, *MNRAS*, 406, 1853, [0909.1189]
 Hardy, B. 1998, *Proceedings in Third International Symposium on Humidity and Moisture*, 1, 214
 Hunter, J. D. 2007, *Computing In Science & Engineering*, 9, 90
 Jones, A., Walker, K. A., Jin, J. J., et al. 2012, *Atmospheric Chemistry and Physics*, 12, 5207
 Lancaster, K., Birkinshaw, M., Gawroński, M. P., et al. 2011, *MNRAS*, 418, 1441, [1106.3766]
 Lawrence, M. G. 2005, *Bull. Amer. Meteor. Soc.*, 86, 225
 Lew, B., Birkinshaw, M., Wilkinson, P., & Kus, A. 2015, *J. Cosmology Astropart. Phys.*, 2, 4, [1410.3660]
 Liljegren, J. C., Clothiaux, E. E., Mace, G. G., Kato, S., & Dong, X. 2001, *J. Geophys. Res.*, 106, 14485
 Murphy, D. M. & Koop, T. 2005, *Q. J. R. Meteorol. Soc.*, 131, 1539
 NASA. 1976, *U.S. Standard Atmosphere, 1976, Tech. rep.*, U.S. Government Printing Office Washington, D.C.
 Paine, S. 2012, *Smithsonian Astrophysical Observatory, SMA technical memo 152 v.7.2*
 Paine, S. 2015, private communication
 Paul, J., Fortuin, F., & Kelder, H. 1998, *J. Geophys. Res.*, 103, 31709
 Peel, M. 2010, *ArXiv e-prints*, [1006.2760]
 Peixoto, J. & Oort, A. H. 1996, *J. Climate*, 9, 3443
 Radford, S. J. & Holdaway, M. A. 1998, in *Society of Photo-Optical Instrumentation Engineers (SPIE) Conference Series*, Vol. 3357, *Advanced Technology MMW, Radio, and Terahertz Telescopes*, ed. T. G. Phillips, 486–494
 Rees, D. 1988, *Advances in Space Research*, 8
 Rees, D. 1992, *Planet. Space Sci.*, 40, 555
 Rees, D., Barnett, J. J., & Labitzke, K. 1990, *Advances in Space Research*, 10
 Schoenberg, E. 1929, "Theoretische Photometrie" in *Hdb. d. Astrophys. Bd. II/1*, ed. B. Springer
 Sioris, C. E., Zou, J., McElroy, C. T., McLinden, C. A., & Vömel, H. 2010, *Advances in Space Research*, 46, 642
 Smirnov, A., Holben, B., Eck, T., Dubovik, O., & Slutsker, I. 2000, *Remote Sensing of Environment*, 73, 337
 Soden, B. J. & Lanzante, J. R. 1996, *J. Climate*, 9, 1235
 Sonntag, D. 1990, *Z. Meteorol.*, 40, 340
 Thomason, L. W., Burton, S. P., Iyer, N., Zawodny, J. M., & Anderson, J. 2004, *Journal of Geophysical Research (Atmospheres)*, 109, 6312
 Velasco, V. A., Toon, G. C., Blavier, J.-F. L., et al. 2011, *Journal of Geophysical Research: Atmospheres*, 116, n/a, d06306
 Walker, K. A., Randall, C. E., Trepte, C. R., Boone, C. D., & Bernath, P. F. 2005, *Geophysical Research Letters*, 32, n/a, 116S04
 Wilson, T. L., Rohlf, K., & Hüttemeister, S. 2009, *Tools of Radio Astronomy* (Springer-Verlag)
 Woś, A. 2010, *Klimat Polski w drugiej połowie XX wieku* (Wydawnictwo Naukowe UAM)
 WOUDC. 1961, *World Ozone and Ultraviolet Radiation Data Centre*, <http://www.woudc.org>